Title

Cannabinol inhibits oxytosis/ferroptosis by directly targeting mitochondria independently of cannabinoid receptors

Authors

Liang, Zhibin
Soriano-Castell, David
Kepchia, Devin
et al.

Publication Date

2022-02-01

DOI

10.1016/j.freeradbiomed.2022.01.001

Peer reviewed

HHS Public Access

Author manuscript

Free Radic Biol Med. Author manuscript; available in PMC 2023 February 20.

Published in final edited form as:

Free Radic Biol Med. 2022 February 20; 180: 33–51. doi:10.1016/j.freeradbiomed.2022.01.001.

Cannabinol inhibits oxytosis/ferroptosis by directly targeting mitochondria independently of cannabinoid receptors

Zhibin Liang[a,b,*], **David Soriano-Castell**[a], **Devin Kepchia**[a], **Brendan M. Duggan**[c], **Antonio Currais**[a], **David Schubert**[a,b], **Pamela Maher**[a,*]

[a]Cellular Neurobiology Laboratory, The Salk Institute for Biological Studies, 10010 North Torrey Pines Road, La Jolla, California 92037, United States

[b]The Paul F. Glenn Center for Biology of Aging Research, The Salk Institute for Biological Studies, 10010 North Torrey Pines Road, La Jolla, California 92037, United States

[c]Skaggs School of Pharmacy and Pharmaceutical Sciences, University of California, San Diego, 9500 Gilman Drive, La Jolla, California 92093, United States

Abstract

The oxytosis/ferroptosis regulated cell death pathway recapitulates many features of mitochondrial dysfunction associated with the aging brain and has emerged as a potential key mediator of neurodegeneration. It has thus been proposed that the oxytosis/ferroptosis pathway can be used to identify novel drug candidates for the treatment of age-associated neurodegenerative diseases that act by preserving mitochondrial function. Previously, we identified cannabinol (CBN) as a potent neuroprotector. Here, we demonstrate that not only does CBN protect nerve cells from oxytosis/ferroptosis in a manner that is dependent on mitochondria and it does so independently of cannabinoid receptors. Specifically, CBN directly targets mitochondria and preserves key mitochondrial functions including redox regulation, calcium uptake, membrane potential, bioenergetics, biogenesis, and modulation of fusion/fission dynamics that are disrupted following induction of oxytosis/ferroptosis. These protective effects of CBN are at least partly mediated by the promotion of endogenous antioxidant defenses and the activation of AMP-activated protein kinase (AMPK) signaling. Together, our data highlight the potential of

[*]To whom correspondence should be addressed: Cellular Neurobiology Laboratory, The Salk Institute for Biological Studies, 10010 North Torrey Pines Road, La Jolla, California 92037, United States. zliang@salk.edu (Dr. Zhibin Liang), pmaher@salk.edu (Dr. Pamela Maher).

Author Contributions

ZL, DS, and PM conceived the project and designed the experiments. ZL, DS-C, DK, BMD, AC, DS, and PM conducted and assisted the experiments, and performed the data analysis and interpretation. ZL wrote the manuscript. All authors provided critical feedback and edited and approved the final manuscript.

Declaration of Competing Interest

The authors declare no conflicts of interest.

Supplementary Material

qPCR data for CB1/CB2 in HT22 cells, cytotoxicity profiles of CBN in different cell lines, mitochondrial membrane potential in different cell lines, Western blotting of mitochondrial markers in HT22 mt-GFP and mt-GFP/mCherry-Parkin cell lines with/without FCCP induction, 1D/2D NMR spectra of CBN, and structures of the reference compounds.

mitochondrially-targeted compounds such as CBN as novel oxytotic/ferroptotic inhibitors to rescue mitochondrial dysfunction as well as opportunities for the discovery and development of future neurotherapeutics.

Graphical Abstract

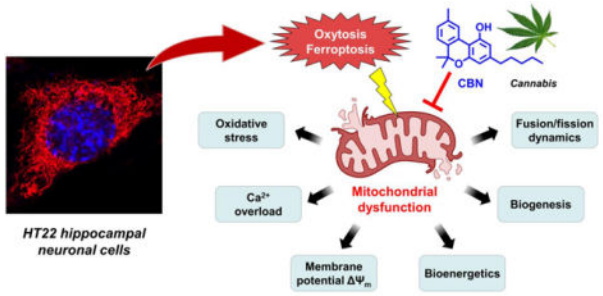

Keywords

Antioxidant defense; cannabinoid; mitochondrial dysfunction; oxytosis/ferroptosis; neurodegenerative disease; aging; neurotherapeutics; AMPK

Introduction

Perhaps the greatest challenge in modern medicine is to enhance healthy aging and thereby prevent or cure the diseases of aging. Aging leads to progressive and detrimental changes in the brain, and old age is the greatest risk factor and likely a driving force for most neurodegenerative diseases including Alzheimer's disease (AD), Parkinson's disease (PD), and Huntington's disease (HD) [1].

Energy production from glucose metabolism supports the majority of brain activity but declines with age and to a greater extent in neurodegenerative diseases [2]. Most of the cerebral energy derived from glucose oxidation is produced in mitochondria. The current consensus is that mitochondrial inefficiency and/or dysfunction in the brain with aging appears to be one of the pathophysiological commonalities contributing to neurodegeneration [3]. It is also evident that an imbalance in the redox status of mitochondria with aging drives the surge in cellular oxidative stress and accumulation of oxidized/misfolded proteins in the brain that exacerbate neurodegenerative processes [2, 4]. Therefore, age-dependent changes in mitochondrial function need to be taken into account in order to translate the biology of aging into novel neurotherapeutics [5–7].

Oxytosis/ferroptosis is a novel non-apoptotic, regulated cell death pathway that recapitulates many features of mitochondrial dysfunction associated with neuronal cell death and has been implicated in age-associated neurodegenerative diseases [6, 8–10]. However, the fundamental mechanisms by which mitochondrial signaling and phenotypes are altered in the context of oxytosis/ferroptosis and whether pharmacological maintenance of mitochondrial homeostasis can protect against oxytosis/ferroptosis are not fully understood.

Aiming to identify new drug candidates from natural products that preserve mitochondrial function in disease, we have focused on medicinal plants with available ethnopharmacological documentation [6, 11]. *Cannabis sativa* (known as marijuana) has been used medicinally in humans for thousands of years [12, 13], yet it has not been extensively examined as a potential source of drug candidates for neurodegenerative diseases [14]. For decades, research on medical cannabis has focused mainly on the major phytocannabinoids, namely tetrahydrocannabinol (THC) and cannabidiol (CBD), for their pharmacological and clinical applications [15–18]. Relatively little scientific knowledge has yet been curated for the minor but structurally diverse phytocannabinoids that are rich in the *Cannabis* plant [19, 20]. Psychoactive phytocannabinoids such as THC are unlikely to be viable drug candidates for most chronic neurodegenerative diseases due to their potential adverse effects, psychosis risks, drug abuse and dependence, as well as legislative regulations worldwide [21]. However, the non-psychoactive counterparts have not been fully explored as therapeutic options for age-associated neurodegenerative diseases.

Recently, we screened a series of phytocannabinoids with both psycho- and non-psychotropic activities using a preclinical platform based on phenotypic screening assays that recapitulate different cellular toxicities and stresses associated with the aging brain that are characterized by mitochondrial dysfunction [22, 23]. Many phytocannabinoids were found to be highly protective in these cell-based assays. Among them, the non-psychoactive phytocannabinoid, cannabinol (CBN), showed a sub-micromolar potency in multiple screens including the oxytosis/ferroptosis assay. Specifically, CBN was able to reduce cellular oxidative stress, protect from the loss of energy and trophic support, and remove intraneuronal β-amyloid in neuronal cells [22], suggesting its merits for further study. Although CBN was identified as a potent inhibitor of oxytosis/ferroptosis, how it exerts its protective actions and whether it acts through mitochondria were unknown.

Herein, we analyzed the changes in mitochondrial phenotypes induced by oxytotic/ferroptotic insults and investigated the mechanism of action of CBN by assessing its effects on key physiological parameters of mitochondria in the context of oxytosis/ferroptosis in a hippocampal nerve cell line. We demonstrate that CBN inhibits oxytosis/ferroptosis by directly targeting mitochondria and restoring impaired mitochondrial function independently of cannabinoid receptor signaling. Our data not only support the therapeutic potential of CBN for the treatment of age-associated neurodegenerative diseases but also reveal new insights into the role of mitochondria in oxytotic/ferroptotic cell death.

Material and Methods

Chemicals and Reagents.

All solvents and reagents were purchased from commercial sources and were used without further purification. CBN was synthesized in-house. Olivetol, citral, *n*-butylamine, iodine, Na_2SO_3, ethyl acetate, petroleum ether, toluene, glutamate, RSL3, carbonyl cyanide-4-(trifluoromethoxy)phenylhydrazone (FCCP), Trolox, ABTS, potassium persulfate, ferrous sulfate, ferrozine, HEPES, cOmplet protease inhibitor cocktail, PhosSTOP phosphatase inhibitor cocktail, and Nonidet P-40 were from Sigma-Aldrich (Saint Louis, MO). Dowex 50WX8 (Cat# AAAL13921) was from VWR (Radnor, PA). Ferrostatin, MitoQ, and STY-

BODIPY (Cat# 27089) were from Cayman Chemical (Ann Arbor, MI). Seahorse XFe96 FluxPak (Cat# 102416) and Seahorse XF Cell Mito Stress Test Kit (Cat# 103015) were from Agilent Technologies (Santa Clara, CA). Calcium indicators Rhod-2 AM (Cat# R1244) and Fluo-4 AM (Cat# F14201), CellROX Green Reagent (Cat# C10444), MitoSOX Red Mitochondrial Superoxide Indicator (Cat# M36008), C11-BODIPY Lipid Peroxidation Sensor (Cat# D3861), MitoTracker Orange CM-H_2TMRos (Cat# M7511), NucBlue Live Cell Stain Hoechst 33342 Reagent (Cat# R37605), CyQUANT Direct Cell Proliferation Assay Kit (Cat# C35011), Pierce BCA Protein Assay Kit (Cat# 23227), Cell Lysis Buffer (Cat# FNN0011), SuperSignal West Pico PLUS Chemiluminescent Substrate (Cat# 34578), HyperSep Silica Cartridge (Cat# 60108-712) were from Thermo Fisher Scientific (Waltham, MA). JC-10 Mitochondrial Membrane Potential Assay Kit (Cat# ab112134) was from Abcam (Burlingame, CA). Criterion XT Bis-Tris Protein Gradient Gel (Ca# 3450125), XT MOPS Running Buffer (Cat# 1610788), Trans-Blot Turbo RTA Transfer Kit (Cat# 1704275), Precision Plus Protein Standards (Cat# 1610373) were from Bio-Rad (Hercules, CA).

General Instrumental Analysis.

Optical absorbance and fluorescence were measured on a SpectraMax M5 Multi-Mode microplate reader (Molecular Devices, San Jose, CA).

Microscopy.

Brightfield, phase contrast, and fluorescence microscopic images were acquired on an IX51 inverted microscope (Olympus Corporation, Tokyo, Japan) with an INFINITY3 monochrome CCD camera (Teledyne Lumenera, Ontario, Canada). Super-resolution microscopic images were acquired on a Zeiss LSM 880 rear port laser scanning confocal and Airyscan FAST microscope (Carl-Zeiss, Oberkochen, Germany). Image processing and analysis were performed with microscope software packages ZEN Black and ImageJ/Fiji.

Mass Spectrometry (MS).

High-resolution mass spectrometric data were obtained on a Thermo Q-Exactive Quadrupole-Orbitrap mass spectrometer in positive mode. Samples were diluted with a 1:1 mixture of methanol and water containing 0.1% formic acid and then introduced by direct electrospray infusion. Accurate masses of all analytes were obtained from the pseudo-molecule $[M+H]^+$ and were within 5 ppm mass error. Full MS scans were recorded for the 150–750 m/z range. MS/MS fragmentation was achieved by higher-energy collisional dissociation (HCD) at normalized collision energy settings between 10 and 30%.

Nuclear magnetic resonance (NMR).

^1H, ^{13}C and 2D NMR data were collected at 298 K on a 600 MHz Bruker Avance III spectrometer fitted with a 1.7 mm triple resonance cryoprobe with z-axis gradients using TopSpin 3.6.0. NMR spectra were referenced to the residual solvent signal (δ_H 7.26, δ_C 77.2 for chloroform-*d*) with chemical shifts reported in δ units (ppm). Resonance multiplicities are denoted s, d, t, q, m, and br for singlet, doublet, triplet, quartet, multiplet, and broad, respectively. 2D HSQC and HMBC NMR spectra were collected using modified versions of

the Bruker pulse sequences hsqcedetgpsisp2.3 and hmbcctetgpl3ndsp, which incorporated an ASAP module to enable faster data acquisition [24]. Spectral widths were 12 ppm for the ^{1}H dimensions, 160 ppm for the HSQC ^{13}C dimension and 250 ppm for the HMBC ^{13}C dimension. For the HSQC spectra 8 scans and 256 t_1 increments were used. For the HMBC spectra 32 scans and 512 t_1 increments were used. Spectra were analyzed using Mnova.

Total Synthesis of Cannabinol (CBN).

A total synthetic protocol was conducted according to a prior method with modifications [25]. To a stirred solution of olivetol (1 g, 5.54 mmol), citral (910 μL, 5.5 mmol) and *n*-butylamine (530 μL, 5.5 mmol) were added in toluene (50 mL). The mixture was refluxed for 16 hr, and then cooled to room temperature. After Dowex 50WX8 (1 g) was added, the solution was stirred for 30 min at room temperature then filtered. To the filtered solution, iodine (2.8 g, 11 mmol) was added, and the mixture was refluxed for an additional 5 hr. The reaction solution was quenched by adding saturated Na_2SO_3, extracted with ethyl acetate and then evaporated to dryness with a rotatory evaporator. The residue was reconstituted in 5% ethyl acetate/petroleum ether and then eluted on a HyperSep silica column (10 g) using the same solvents to give CBN as a yellow oil (1.3 g, 4.19 mmol, 76% total yield). The identity and purity of CBN were confirmed by high-resolution NMR and mass spectrometry analyses.

Cell Culture.

HT22 mouse hippocampal nerve cells were cultured in high-glucose Dulbecco's modified Eagle's medium (DMEM) (Invitrogen, Cat# 11995065, Carlsbad, CA) supplemented with 10% fetal bovine serum (FBS) (Invitrogen, Carlsbad, CA) and 1% antibiotics including penicillin and streptomycin (Invitrogen Cat# 10378016, Carlsbad, CA). Cell cultures were incubated at 37 °C in a fully humidified atmosphere containing 10% CO_2.

SH-SY5Y neuroblastoma cells were cultured in 1:1 (v/v) DMEM/F12 medium (Invitrogen, Cat# 11330032, Carlsbad, CA) supplemented with 1% non-essential amino acids (Invitrogen, Cat# 11140050), 10% FBS, and 1% antibiotics including penicillin and streptomycin. Cell cultures were incubated at 37 °C in a fully humidified atmosphere containing 10% CO_2.

BV2 microglial cells were cultured in low glucose DMEM supplemented with GlutaMAX (Invitrogen, Cat# 10567014, Carlsbad, CA), 1 mM sodium pyruvate, 10% FBS, and 1% antibiotics including penicillin and streptomycin. Cell cultures were incubated at 37 °C in a fully humidified atmosphere containing 10% CO_2.

Embryonic Cortical Neuron Extraction.

Primary cortical neurons were prepared from embryonic day 17 Sprague-Dawley rat pups and used at 7 days *in vitro* (7DIV) as previously described [26]. Neurons were dissociated from the cortex and maintained in Neurobasal-A medium (Invitrogen, Cat# 10888022, Carlsbad, CA) supplemented with B-27 Supplement (Invitrogen, Cat# 17504044, Carlsbad, CA), 2 mM glutamine, and 1% antibiotics including penicillin and streptomycin. Cell cultures were incubated at 37 °C in a fully humidified atmosphere containing 10% CO2. All

animal procedures were approved by the Salk Institute's Institutional Animal Care and Use Committee.

Generation of Stable HT22 mt-GFP and mt-GFP/mCherry-Parkin Cell Lines.

The procedure was carried out as described [27]. The mitochondrially targeted green fluorescent protein (GFP) plasmid was transfected into HT22 cells using GenJet In Vitro DNA Transfection Reagent (Ver. II) (SignaGen laboratories, Cat# SL100489, Frederick, MD) and stably fluorescent cell colonies were then isolated. The resulting stable line was transfected with a plasmid expressing mCherry-Parkin and a similar procedure was performed to isolate cells stably coexpressing both constructs.

Cell Protein Extraction.

The procedure was carried out as described [28]. HT22 cells were seeded onto 10 cm dishes at a density of 400,000 cells/dish in DMEM supplemented with 10% FBS and 1% antibiotics, and then exposed to the desired treatments. For total protein extracts, HT22 cells were washed with ice-cold phosphate buffered saline (PBS) and lysed with cell extraction buffer containing 10 mM Tris, pH 7.4, 100 mM NaCl, 1 mM EDTA, 1 mM EGTA, 1 mM NaF, 20 mM $Na_4P_2O_7$, 2 mM Na_3VO_4, 1% Triton X-100, 10% glycerol, 0.1% sodium dodecyl sulfate (SDS), 0.5% sodium deoxycholate, a protease inhibitor cocktail, and a phosphatase inhibitor cocktail followed by centrifugation (14000*g*) for 30 min at 4 °C. For nuclear extracts, HT22 cells were washed with ice-cold PBS, incubated with a nuclear fractionation buffer containing 10 mM HEPES, pH 7.9, 10 mM KCl, 0.1 mM EDTA, 0.1 mM EGTA, 1 mM DTT, 1 mM Na_3VO_4, a protease inhibitor cocktail, and a phosphatase inhibitor cocktail on ice for 15 min, then Nonidet P-40 at a final concentration of 0.6% was added to the buffer. Cells were vortexed, and the nuclei pelleted by centrifugation (1000*g*) for 10 min at 4 °C. Nuclear proteins were extracted by sonication of the nuclear pellet in nuclear fractionation buffer followed by centrifugation (14000*g*) for 30 min at 4 °C. The resulting supernatants of total/nuclear protein extracts were stored at −80°C until analysis. Concentrations of the harvested proteins were determined by the BCA protein assay.

Immunoblotting.

Western blots were carried out as described [29]. Laemmli sample buffer with 2% β-mercaptoethanol was added to the samples and then boiled for 5 min prior to SDS-PAGE. Equal amounts of cellular protein for each sample (10 μg per lane) were resolved by 4–12% gradient Criterion XT Precast Bis-Tris Gels (Bio-Rad, Hercules, CA) and transferred onto PVDF membranes with a Trans-Blot Turbo System (Bio-Rad, Hercules, CA). The membranes were blocked with 5% skim milk in TBST (20 mM Tris buffer, pH 7.5, 0.5 M NaCl, 0.1% Tween 20) for 1 hr at room temperature and incubated overnight at 4°C with the diluted primary antibody in 5% BSA in TBST. After washes with TBST, the membranes were incubated with horseradish peroxidase-conjugated goat anti-rabbit or anti-mouse secondary antibodies (Bio-Rad, Hercules, CA) diluted 1:5000 in 5% skim milk in TBST. For all primary antibodies, the same membrane was re-probed for β-actin or an antiserum reacting with the total protein. After additional washing, protein bands were detected using the SuperSignal West Pico PLUS Chemiluminescent Substrate, and visualized with a ChemiDoc MP Imaging System (Bio-Rad, Hercules, CA). Band density was quantified

densitometrically with Image Lab software (Bio-Rad, Hercules, CA). Relative protein expression was normalized to β-actin band density. Each Western blot was performed three to six times with independent protein samples (n = 3–6).

The primary antibodies used were from the following suppliers: antibodies against OPA1 (Cat# 80471, 1:3000), MFN2 (Cat# 9482, 1:3000), DRP1 (Cat# 8570, 1:3000), MFF (Cat# 84580, 1:3000), TOM20 (Cat# 42406, 1:3000), VDAC (Cat# 4661, 1:3000), SIRT1 (Cat# 9475, 1:3000), total AMPKα (Cat# 5831, 1:3000), phosphoThr172-AMPKα (Cat# 2535, 1:1000), SOD2 (Ca# 13141, 1:3000), GPX4 (Cat# 52455, 1:3000), MCU (Cat# 14997, 1:3000), HSP60 (Cat# 12165, 1:3000), β-actin (Cat# 4970, 1:3000) were from Cell Signaling Technology (Danvers, MA); antibodies against TFAM (Ca# ab131607, 1:3000), NRF1 (Cat# ab175932, 1:3000), total OXPHOS (Cat# ab ab110413, 1:3000) were from Abcam (Cambridge, MA); antibodies against ATF4 (Cat# sc-200, 1:1000), Nrf2 (Cat# sc-13032, 1:1000) were from Santa Cruz Biotechnology (Dallas, TX); anti-HO-1 (Cat# SPA-896, 1:3000) was from Stressgen (Victoria, BC, Canada); anti-PGC-1α (Cat# AB3242, 1:3000) was from Sigma-Aldrich (Saint Louis, MO). Horseradish peroxidase-conjugated secondary antibodies (Cat# 1706515, and 1706516) were from Bio-Rad (Hercules, CA).

Oxytosis Assay.

The assay procedure was previously described [29]. HT22 cells were seeded at 3,000 cells/well in 96-well tissue culture plates in DMEM plus 10% FBS and 1% antibiotics. After 24 hr of plating, the cells were pretreated with different concentrations of the test compounds or a vehicle control for 1 hr followed by coincubation with 5 mM glutamate to initiate the cell death cascade. After 16 hr of treatment, cell viability was measured by the 3-(4,5-dimethylthiazol-2-yl)-2,5-diphenyltetrazolium bromide (MTT) assay. Optical absorbance was measured at 570 nm on a SpectraMax M5 microplate reader. Samples were analyzed in eight to sixteen wells per independent experiment (n = 8–16). Results are presented as the percentage of the controls with vehicle alone. Results were verified by visual inspection of the cells under a microscope.

Ferroptosis Assay:

The assay procedure was previously described [29]. HT22 cells were seeded at 3,000 cells/well in 96-well tissue culture plates in DMEM plus 10% FBS and 1% antibiotics. After 24 hr of plating, the cells were pretreated with different concentrations of test compounds or a vehicle control for 1 hr followed by coincubation with 50 nM RSL3 to induce the cell death cascade. After 16 hr of treatment, cell viability was measured by the MTT assay. Optical absorbance was measured at 570 nm on a SpectraMax M5 microplate reader. Samples were analyzed in eight to sixteen wells per independent experiment (n = 8–16). Results are presented as the percentage of the controls with vehicle alone. Results were verified by visual inspection of the cells under a microscope.

Reactive Oxygen Species Measurement.

The assay procedure was previously described [30]. HT22 cells were seeded onto 96-well black walled plates at a density of 5,000 cells/well in DMEM supplemented with 10% FBS and 1% antibiotics. After the desired treatments, whole cell ROS and mitochondrial

superoxide ROS were detected with CellROX Green reagent (Ex/Em = 485/520 nm) and MitoSOX Red reagent (Ex/Em = 510/580 nm), respectively. Experiments were performed according to the manufacturer's instructions. Fluorescence was measured on a SpectraMax M5 microplate reader. Data were normalized for total protein/well. Each condition was analyzed in sixteen wells per independent experiment (n = 16). Results are presented as the percentage of the controls with vehicle alone. Results were verified by live-cell imaging under a fluorescence microscope.

Lipid Peroxidation Measurements.

The assay procedures were previously described with adaptations [31, 32]. HT22 cells were seeded onto 96-well black walled plates at a density of 3,000 cells/well in DMEM supplemented with 10% FBS and 1% antibiotics. After the desired treatments, cells were labeled with 2.5 μM C11-BODIPY 581/591 (oxidized form Ex/Em = 488/520 nm) at 37°C for 2 hr. Experiments were performed according to the manufacturer's instructions. Fluorescence was measured on a SpectraMax M5 microplate reader. Data were normalized for total protein/well. Each condition was analyzed in twelve wells per independent experiment (n = 12). Results are presented as the percentage of the controls with vehicle alone. Results were verified by live-cell imaging under a fluorescence microscope.

For the cell-free, liposome-based assay, STY-BODIPY (1.5 μM) and liposomes of egg-PC (1 mM) (Avanti Polar Lipids Inc, Cat# 840051P, AL) in TBS (pH 7.4) were added to an opaque 96-well plate. This was followed by the addition of test compounds (10 μM). The plate was incubated for 30 min at 37°C and then vigorously mixed for 5 min. The autoxidation was initiated by the addition of V-70 (0.5 mM) (Fujifilm Wako, Cat# 001-70078, Japan), followed by additional mixing for 5 min. Data were acquired at Ex/Em = 488/518 nm every 15 min at 37°C on a SpectraMax M5 microplate reader. Data were transformed into [ox-STY-BODIPY] by taking the raw fluorescent values of the saturated curve of control DMSO and dividing them by the initial concentration of reduced STY-BODIPY (1.5 μM). Samples were analyzed in quadruplicate in four independent experiments (n = 4).

Trolox Equivalent Antioxidant Capacity (TEAC) Assay.

The assay was conducted as previously described [33]. Briefly, an aqueous 2,2'-azino-bis(3-ethylbenzothiazoline-6-sulfonic acid) (ABTS) solution (7 mM) was treated with potassium persulfate ($K_2S_2O_8$) (2.5 mM) overnight at room temperature in the dark and diluted in water to an OD value of 0.7 at 734 nm. 190 μL of the diluted ABTS solution was added to a 96-well plate containing 10 μL of test compounds or Trolox at the desired concentrations. The plate was vigorously mixed and incubated for 4 min at room temperature in the dark. Optical absorbance was measured at 734 nm on a SpectraMax M5 microplate reader. The decrease in absorbance of the ABTS radical cation indicates the presence of antioxidants. Samples were analyzed in eight wells per independent experiment (n = 8). The TEAC values of each sample are presented as the percentage of the standard Trolox at 5 μM.

Iron (Fe^{2+}) Binding Assay.

Ferrous iron binding was measured by the ferrozine method as described [34]. Briefly, test samples at the desired concentrations were mixed with 5 μM ferrous sulfate ($FeSO_4$) in 100

μL of 50 mM HEPES, pH 7.5 in a 96-well plate. After 2 min, 50 μL of 5 mM ferrozine was added and the optical absorbance at 562 nm was measured on a SpectraMax M5 microplate reader. Each sample was analyzed in eight wells per independent experiment (n = 8). Iron binding capacities are presented as the percentage of the vehicle controls without (100%) or with iron (0%).

Total GSH Measurements.

The assay was conducted as previously described [29]. HT22 cells were seeded onto 35 mm dishes at a density of 70,000 cells/dish in DMEM supplemented with 10% FBS and 1% antibiotics. After the desired treatments, the cells were scraped into ice-cold PBS and the cell pellets collected by centrifugation (500*g*). The pellets were resuspended in PBS and 10% sulfosalicylic acid was added at a final concentration of 3.3% to the cells. Proteins were pelleted by centrifugation and the supernatant neutralized. Total GSH was determined by the recycling assay based on the reduction of 5,5-dithiobis(2-nitrobenzoic acid) with glutathione reductase and NADPH and normalized to protein recovered from the acid-precipitated pellet by treatment with 0.2 N NaOH at 37 °C overnight and measured by the BCA protein assay (Pierce, Rockford, IL, USA). Samples were analyzed in four dishes per independent experiment (n = 4).

Calcium Measurements.

The assay procedure was previously described [35]. HT22 cells were seeded onto 96-well black walled plates at a density of 5,000 cells/well in DMEM supplemented with 10% FBS and 1% antibiotics. After the desired treatments, Ca^{2+} levels were detected with Fluo-4 AM (Ex/Em = 494/516 nm) and Rhod-2 AM (Ex/Em = 552/581 nm) calcium indicator dyes specific to cytosol and mitochondria, respectively. Fluorescence was measured on a SpectraMax M5 microplate reader. Experiments were performed according to the manufacturer's instructions. Data were normalized for total protein/well. Each condition was analyzed in sixteen wells per independent experiment (n = 16). Results are presented as the percentage of the controls with vehicle alone. Results were verified by live-cell imaging under a fluorescence microscope.

Seahorse XF Analysis.

The assay procedure was previously described [30]. Cellular oxygen consumption rates (OCR) were assayed with a XF Cell Mito Stress Test Kit using a Seahorse XFe96 Extracellular Flux Analyzer (Seahorse Bioscience, North Billerica, MA). Complete Seahorse XF DMEM assay medium was supplemented with 10 mM glucose, 1 mM pyruvate and 2 mM L-glutamine, at pH 7.4. Mitochondrial ETC inhibitors were used at the following concentrations: 1.5 μM oligomycin, 2 μM FCCP, and 0.5 μM of a 1:1 mixture of rotenone and antimycin A. Analyses were conducted using Wave software and XF Report Generators (Agilent Technologies). The sensor cartridge for the XFe analyzer was hydrated overnight at 37 °C before the experiment. OCR data were normalized for total protein/well. Each condition was analyzed in 20–40 wells per independent experiment (n = 20–40).

For HT22 cells, 3,000 cells/well were seeded onto the Seahorse XFe96 plates under normal culture condition as described above. The next day, cells were pretreated with CBN at the

desired concentrations for 1 hr followed by addition of RSL3 (50 nM) and coincubation for 16 hr. Immediately before the assay, the culture medium in the plates was replaced with complete Seahorse XF DMEM assay medium. The plates were incubated for 1 hr at 37 °C prior to the XF Cell Mito Stress tests according to the manufacturer's instructions.

For primary cortical neurons, the cells were seeded onto poly-L-ornithine coated Seahorse XFe96 plates at a density of 20,000 cells/well under the culture condition as described above and incubated for two days. On day 3, the cells were pretreated with CBN at the desired concentrations for 1 hr followed by addition of RSL3 (50 nM) and coincubation for 16 hr. Immediately before the assay, the culture medium in plates was replaced with complete Seahorse XF DMEM assay medium. The plates were incubated for 1 hr at 37 °C prior to the XF Cell Mito Stress tests according to the manufacturer's instructions.

Mitochondrial Membrane Potential Assay.

The assay procedure was previously described [36]. Cells seeded at 5,000 cells/well onto 96-well black walled plates were treated with test compounds at the desired concentrations under the culture condition described above. The mitochondrial uncoupler FCCP at 2 μM was used as a reference control. After the desired treatments for 4 hr, the cells were subjected to a JC-10 mitochondrial membrane potential assay according to the manufacturer's instruction. Fluorescence intensities (Ex/Em =490/525 nm, and Ex/Em = 540/590 nm) of each well were monitored on a SpectraMax M5 microplate reader. The ratio of fluorescence intensity (590/525 nm) was used to determine the mitochondrial membrane potential ($\Delta\Psi m$). Decreasing ratios indicate mitochondrial membrane depolarization. Samples were analyzed in eight to sixteen wells per independent experiment (n = 8–16). Results were verified by live-cell imaging under a fluorescence microscope.

Quantitative Reverse Transcription PCR (qPCR) Analysis.

HT22 cells were seeded onto 60 mm dishes at a density of 140,000 cells/dish in DMEM supplemented with 10% FBS and 1% antibiotics. After the desired treatments, total RNA was extracted using the RNeasy Mini Kit (Qiagen, Cat# 74104, Hilden, Germany). cDNA was synthesized using SuperScript III FirstStrand Synthesis System for qPCR (Invitrogen, Cat# 18080051, Carlsbad, CA). Amplification was performed with TaqMan Fast Advanced Master Mix (ThermoFisher Scientific, Cat# 4444556, Carlsbad, CA) using a QuantStudio 3 Real-Time PCR Systems (ThermoFisher Scientific, CA). The primer pairs were used as follows: *CNR1* (Forward, 5'-AAGTCGATCTTAGACGGCCTT-3'; Reverse, 5'-TCCTAATTTGGATGCCATGTCTC-3'); *CNR2* (Forward, 5'-ACGGTGGCTTGGAGTTCAAC-3'; Reverse, 5'-GCCGGGAGGACAGGATAAT-3'). The expression of the *GAPDH* gene was measured for normalization. The mouse Mitochondrial DNA Copy Number Kit was used (Detroit R&D, Cat# MCN3, Detroit, MI) according to the manufacturer's instructions. Relative fold change was calculated using the $2^{(-\Delta\Delta Ct)}$ method. Samples were analyzed in three dishes per independent experiment (n = 3).

MitoTracker Assay.

The assay procedure was previously described [37]. HT22 cells were seeded onto 96-well black walled plates at a density of 5,000 cells/well in DMEM supplemented with 10%

FBS and 1% antibiotics. After the desired treatments, MitoTracker Orange CM-H_2TMRos (Ex/Em = 554/576 nm) and Hoechst 33342 (Ex/Em = 360/460 nm) dyes were added to the cells and incubated under the same culture condition for 2 hr. Fluorescence was measured on a SpectraMax M5 microplate reader. Experiments were performed according to the manufacturer's instructions. Data were normalized for total protein/well. Each condition was analyzed in sixteen wells per independent experiment (n = 16). Results are presented as the percentage of the controls with vehicle alone. Results were verified by live-cell imaging under a fluorescence microscope.

Mitochondrial Network Morphology Analysis.

HT22 mt-GFP cells were seeded at 20,000 cells/well on glass coverslips in 24-well plates in DMEM supplemented with 10% FBS and 1% antibiotics. The following day, the cells were treated with the test compounds for the desired period of time. After rinsing with PBS, the cells on glass coverslips were fixed with 4% paraformaldehyde (pH 7.4) for 10 min at 37°C. After additional PBS rinses, the coverslips were mounted onto glass microslides with Fluoro-Gel (Electron Microscopy Sciences, Cat#17985-10). Z-stack images of fixed cells were acquired on a Zeiss LSM 880 rear port laser scanning confocal and Airyscan FAST microscope with ZEN Black software to trace and render cells in 3D. The mitochondrial network morphology parameters (n = 20–25 cells/condition) were scored and analyzed with the MiNA module of ImageJ/Fiji software using previously described methods [38].

CyQUANT Cell Proliferation Assay.

HT22 mt-GFP or mt-GFP/mCherry-Parkin cells were seeded onto 96-well black walled plates at a density of 3,000 cells/well in DMEM supplemented with 10% FBS and 1% antibiotics. After overnight incubation, the cells were pretreated with 5 μM FCCP or vehicle for 24 hr followed by the addition of test compounds or vehicle for an additional 16 hr. After the desired treatments, CyQUANT (Ex/Em = 508/560 nm) reagents were added to the cells and incubated for 1 hr. The experiments were performed according to the manufacturer's instructions. Fluorescence was measured on a SpectraMax M5 microplate reader. Each condition was analyzed in eight to twelve wells per independent experiment (n = 8–12). Results are presented as the percentage of the controls with vehicle alone. Results were verified by live-cell imaging under a fluorescence microscope.

Statistical Analysis.

Data are presented as the mean ± SD. The half maximal effective concentration (EC_{50}) was determined from sigmoidal dose response curves with four-parameter regression. The data were analyzed by one-way ANOVA with Tukey's multiple comparison post hoc test or Student's *t* test where appropriate. P values less than 0.05 were considered statistically significant (* $p < 0.05$, ** $p < 0.01$, *** $p < 0.001$, and **** $p < 0.0001$). Analyses were performed using Excel and GraphPad Prism.

Results

Total synthesis of CBN.

Given the federal and state regulations of cannabinoids, CBN was synthesized in-house under a DEA license. The iodine-catalyzed condensation of citral and olivetol (Figure 1) provided an efficient, concise, and inexpensive method for the total synthesis of CBN in gram-scale quantities with a total yield of 76%. The identity of CBN was confirmed by high-resolution nuclear magnetic resonance (NMR) and mass spectrometry (MS) analyses. ^{1}H NMR (600 MHz, $CDCl_3$) δ 8.18 (s, 1H), 7.15 (d, J = 7.9 Hz, 1H), 7.08 (m, 1H), 6.45 (d, J = 1.6 Hz, 1H), 6.29 (d, J = 1.6 Hz, 1H), 5.29 (br s, 1H), 2.53–2.47 (m, 2H), 2.39 (s, 3H), 1.64–1.57 (m, 8H), 1.38–1.25 (m, 4H), 0.90 (t, J = 6.9 Hz, 3H). ^{13}C NMR (75 MHz, $CDCl_3$) δ 154.7, 153.1, 144.7, 137.0, 137.0, 127.7, 127.6, 126.5, 122.7, 110.9, 110.0, 108.8, 77.5, 35.7, 31.6, 30.6, 27.2, 27.2, 22.7, 21.7, 14.2. HR-MS m/z $[M+H]^+$ 311.2009 (calculated for $C_{21}H_{27}O_2^+$, 311.2006, 0.96 ppm error). Collected NMR and MS spectra for CBN were cross-referenced with the reported data in the literature [39]. The purity of CBN was over 95% as determined by quantitative NMR analysis.

CBN inhibits oxytosis/ferroptosis independently of cannabinoid receptors.

Mouse hippocampal HT22 cells are a neuronal cell line that lack cannabinoid receptors (CB1 and CB2, canonical targets of cannabinoids), as verified by qPCR analysis (Supplementary Materials Figure S1) and prior studies [40]. Because CBN was previously identified as a potent protector against multiple insults in HT22 cells [22], we used this cell line to investigate the neuroprotective mechanisms of CBN independently of cannabinoid receptor signaling.

Oxytosis/ferroptosis can be induced by inhibiting the cystine/glutamate antiporter (system Xc-) with glutamate, leading to loss of the endogenous antioxidant glutathione (GSH), excessive calcium influx into mitochondria, production of reactive oxygen species (ROS) from mitochondria, increases in lipid peroxidation across cellular membranes, and ultimately cell death [8, 9]. Oxytosis/ferroptosis can also be triggered by inhibition of glutathione peroxidase 4 (GPX4), a GSH-dependent antioxidant enzyme, with RSL3 [10]. System Xc- and GPX4 are upstream and downstream targets, respectively, in oxytosis/ferroptosis and they play critical roles in this regulated cell death pathway [41]. Thus, we first assessed the neuroprotection by CBN against both glutamate and RSL3 induced cell death in HT22 cells.

Microscopic imaging clearly showed that treatment with CBN at 5 μM for 16 hr did not induce visual changes in cellular morphology compared to the control HT22 cells (Figure 2A–B). However, treatment with a subtoxic dose of glutamate (5 mM) (Figure 2C) or RSL3 (50 nM) (Figure 2D) for 16 hr led to dramatic changes in cellular morphology with large numbers of rounded, shrinking, and detached cells present as compared to the control group (approximately 40–60% cell death). Such changes in morphology are characteristic of oxytosis/ferroptosis and are consistent with previous findings [8, 41]. Pretreatment with 5 μM CBN for 1 hr followed by co-incubation with either glutamate or RSL3 for 16

hr effectively prevented these morphological changes, as nearly all the HT22 cells were healthy, well adhered, and had fine projections similar to the control cells (Figure 2E–F).

Quantitative dose-response measurements of cell viability with the MTT assay also showed that CBN effectively blocked the oxytosis/ferroptosis pathway induced by 5 mM glutamate (Figure 2G) or 50 nM RSL3 (Figure 2H) with the half maximal effective concentration (EC_{50}) values of 1.89 μM and 0.69 μM, respectively. Remarkably, no apparent cytotoxicity by CBN was observed in HT22 cells up to a dose of 200 μM (Figure 2I), although cytotoxicity was noted at concentrations of 500 μM and above. Similar low toxicity profiles for CBN were seen in other cell lines such as PC12 pheochromocytoma cells, SH-SY5Y neuroblastoma cells, BV2 microglia, HepG2 liver cancer cells, and H9C2 cardiomyocytes (Supplementary Materials Figure S2).

Together, these data suggest that CBN is a potential drug lead worthy of further investigation. Therefore, we investigated the mechanism of action of CBN against oxytosis/ferroptosis focusing on oxidative stress and mitochondrial dysfunction.

CBN suppresses mitochondrial oxidative stress in oxytosis/ferroptosis.

Activation of the oxytosis/ferroptosis pathway causes an elevation of oxidative stress, particularly in mitochondria, where mitochondrial ROS (mtROS) contribute to the lipid peroxidation of membranes [9, 42]. We thus first investigated whether CBN is capable of inhibiting the cascade of mitochondrial oxidative stress induced by oxytosis/ferroptosis.

We tested the inhibitory effect of CBN on ROS production/accumulation using two different fluorogenic probes, CellROX and MitoSOX, in live HT22 cells. The CellROX reagent is universal for cellular ROS detection, whereas the MitoSOX reagent is a ROS superoxide indicator specifically targeting mitochondria in live cells. As shown in Figure 3A–B, CBN (5 μM) alone did not affect the redox status of cells or mitochondria following treatment for 16 hr. However, HT22 cells treated with 50 nM RSL3 for 16 hr showed a significant increase in ROS markers in cells and in mitochondria in comparison to the control cells ($p < 0.0001$). Treatment with CBN suppressed the RSL3-induced ROS production at both the cellular and mitochondrial levels.

Because lipid peroxidation and GSH dysregulation are major characteristics of oxytosis/ferroptosis that play key roles in the cell death pathway, we asked whether CBN modulated either of these two events. Ferrostatin, a known oxytotic/ferroptotic inhibitor that prevents lipid autoxidation by trapping peroxyl radicals [43], was used as a reference control. After treatment for 16 hr, neither CBN (5 μM) nor ferrostatin (10 μM) alone changed basal levels of lipid peroxidation in HT22 cells, whereas RSL3 (50 nM) significantly enhanced the cellular lipid peroxidation level by approximately 30% ($p < 0.0001$) (Figure 3C). Treatment with CBN or ferrostatin effectively suppressed the RSL3-induced cellular lipid peroxidation ($p < 0.0001$). Surprisingly, in a cell-free, liposome-based assay of lipid peroxidation (Figure 3D) CBN at 10 μM (a concentration 2-fold higher than in the cell-based assay) showed no inhibition relative to the control indicating that it is not a direct inhibitor of lipid peroxidation. Conversely, ferrostatin at 10 μM showed a potent effect against lipid peroxidation in the cell-free assay. The lack of antioxidant effects of CBN in a cell-free

system is supported by the results of the TEAC assay that measures the total antioxidant capacity of compounds. The TEAC data (Figure 3E) indicate a relatively weak capacity of CBN (5 to 10 μM) to scavenge total free radicals as compared to the standard antioxidant Trolox at 5 μM. Moreover, we ruled out the possibility that CBN acts as an iron chelator in preventing iron-dependent lipid peroxidation [10], as CBN at 5 to 10 μM (Figure 3F) did not show significant Fe^{2+} binding as compared to the known iron chelator deferiprone (5 μM), which also inhibits oxytosis/ferroptosis [32, 44]. In addition, we found that CBN at 5 μM had no impact on the total GSH levels in HT22 cells (Figure 3G) regardless of its strong oxytosis/ferroptosis inhibition at the same concentration.

To further explore the antioxidant effect of CBN, the levels of several proteins known to be involved in endogenous antioxidant defenses, including nuclear erythroid 2-related factor (Nrf2), activating transcription factor 4 (ATF4), heme oxygenase-1 (HO-1), superoxide dismutase 2 (SOD2), and GPX4 [29, 45–47], were examined. Western blotting data (Figure 3H–I) showed that CBN alone at 5 μM was able to stimulate the upregulation of Nrf2, HO-1, SOD2, and GPX4 in HT22 cells. By contrast, RSL3 significantly decreased the expression of Nrf2, ATF4, and GPX4 in HT22 cells, and the effects were particularly substantial for Nrf2 and GPX4 ($p < 0.0001$). Interestingly, CBN at 5 μM counteracted the effects of RSL3 and maintained all four antioxidant proteins (i.e., Nrf2, HO-1, SOD2, and GPX4) at levels similar to the control cells, whereas the effect of CBN on ATF4 was not significant. Mitochondrial heat shock protein 60 (HSP60) is a chaperone that is upregulated in response to mitochondrial stress [48]. We found that HSP60 was significantly upregulated by RSL3, but this increase was suppressed by CBN (Figure 3I). Overall, we found that CBN has a strong antioxidant potential to reduce/neutralize mtROS and lipid peroxides possibly mediated by the activation of cellular antioxidant defenses. Based on these results, we hypothesized that CBN may have direct effects on mitochondria and thus focused our further studies on this important organelle.

CBN maintains mitochondrial calcium homeostasis in oxytosis/ferroptosis.

Mitochondrial Ca^{2+} homeostasis is essential to many neuronal functions. Excessive mitochondrial Ca^{2+} influx is detrimental to the neuron, enhances mtROS production and has been shown to take place during oxytosis/ferroptosis [35, 49]. Therefore, we next examined the impact of CBN on mitochondrial Ca^{2+} homeostasis during oxytosis/ferroptosis.

As shown in Figure 4A–B, incubation of CBN at 5 μM for 16 hr did not affect Ca^{2+} influx in either the cytosol or mitochondria as determined by the calcium indicators Fluo-4 AM and Rhod-2 AM, respectively. On the other hand, RSL3 treatment for 16 hr caused a significant increase in Ca^{2+} in both the cytosol and mitochondria ($p < 0.0001$). Pretreatment with CBN for 1 hr followed by co-incubation with RSL3 maintained basal Ca^{2+} levels in the cytosol and in mitochondria.

The mitochondrial calcium uniporter (MCU) is a key calcium channel located in the mitochondrial inner membrane that mediates the uptake of Ca^{2+} ions into the mitochondrial matrix. MCU dysregulation and malfunction have been implicated in mitochondrial bioenergetic impairment [50] and to a greater extent in neurodegenerative disorders [51]. Therefore, we examined the MCU levels upon compound treatment by Western blotting.

Interestingly, the data (Figure 4C–D) showed that treatment with CBN alone at 5 μM for 16 hr reduced basal MCU expression in HT22 cells while RSL3 upregulated MCU in the cells ($p < 0.0001$), and CBN prevented this increase ($p < 0.0001$). Together, the combined data from the calcium assays and the MCU measurement indicate that CBN can prevent Ca^{2+} overload in mitochondria.

CBN modulates the oxidative phosphorylation (OXPHOS) system and restores mitochondrial bioenergetics.

Mitochondrial bioenergetics are involved in biochemical and molecular pathways of energy production and transformation in cells. Bioenergetics and metabolic regulation are the primary functions of mitochondria, and mitochondrial respiration in the electron transport chain (ETC) produces ATP via the OXPHOS process to fuel a variety of vital cellular functions. Disruption of mitochondrial bioenergetics can thus promote cell damage and death [52].

To assess mitochondrial bioenergetics, cellular respiration profiling was conducted using the Seahorse mitochondrial stress test, where cells were sequentially treated with OXPHOS inhibitors (i.e., oligomycin, FCCP, rotenone, and antimycin A). To determine whether cannabinoid receptors influence mitochondrial respiration, both HT22 nerve cells (cannabinoid receptor-deficient) and embryonic cortical neurons (cannabinoid receptor-expressing) were assayed. Based on a nearly 100% neuroprotection of CBN against 50 nM RSL3 in both HT22 cells and primary neurons (data not shown), CBN was used at 10 μM in this experiment.

The results in HT22 cells (Figure 5A–B) showed that CBN alone partially decreased both basal and maximal mitochondrial respiration, and also partially reduced ATP production. RSL3 at 50 nM almost completely depressed mitochondrial respiration as the oxygen consumption rate (OCR) barely responded to the OXPHOS inhibitors. However, HT22 cells pretreated with 10 μM of CBN followed by RSL3 treatment for 16 hr showed a maintenance of mitochondrial respiration and ATP production. Similar effects of both CBN and RSL3 on OCR profiles and mitochondrial respiration were observed in embryonic cortical neurons (Figure 5C–D) in which cannabinoid receptors are highly expressed [53].

The mitochondrial membrane potential ($\Delta\Psi m$) is generated by the OXPHOS proton pumps (complexes I, III and IV) across the mitochondrial inner membrane, thereby powering ATP production. We tested whether RSL3 or CBN directly affect $\Delta\Psi m$ in HT22 cells. FCCP was used as a reference control because it is an uncoupling agent that decreases the proton gradient of mitochondrial OXPHOS and disrupts $\Delta\Psi m$ in cells [54]. Interestingly, our data (Figure 5E) showed that short-term treatment with RSL3 at 50 nM for 4 hr had no impact on $\Delta\Psi m$. However, treatment with CBN at 5 μM for 4 hr partially decreased $\Delta\Psi m$ by approximately 17% in HT22 cells ($p < 0.0001$), an effect comparable to that of FCCP (2 μM). Co-treatment with CBN and RSL3 showed an effect on $\Delta\Psi m$ depolarization similar to that of CBN alone. The effects of CBN on decreasing $\Delta\Psi m$ were also observed in SH-SY5Y neuroblastoma cells and BV2 microglia (Supplementary Materials Figure S3).

Given these results, we further examined the effect of CBN on the mitochondrial OXPHOS protein complexes. Because mtDNA is known to encode 13 proteins within complexes I, III, IV and V in the mitochondrion, all of which are involved in the OXPHOS process [55], the response of mtDNA copy number to the compound treatments in the cells could offer meaningful information to help elucidate how CBN affects mitochondrial bioenergetics. As shown in Figure 5F, CBN (5 μM) alone did not induce significant changes in mtDNA in HT22 cells. However, treatment with RSL3 at 50 nM for 16 hr significantly increased mtDNA copy number compared with the control cells, and CBN was able to repress the increase in mtDNA by RSL3 and sustain mtDNA at the control level. Consistent with the mtDNA data, Western blotting (Figure 5G–H) also showed that CBN did not exert obvious effects on the protein expression of the OXPHOS complexes I, II, III, and V, but reduced the protein level of complex IV ($p < 0.0001$). In contrast, treatment with RSL3 at 50 nM significantly upregulated all five of the OXPHOS complexes in HT22 cells ($p < 0.0001$). The aberrant upregulation of the OXPHOS complexes by RSL3 was inhibited by CBN with highly significant effects on the levels of complexes I, III, IV, and V ($p < 0.0001$). Collectively, our data show that the restoration of mitochondrial bioenergetics by CBN appears to be mediated in part by the modulation of $\Delta\Psi m$ and the OXPHOS complexes.

CBN promotes mitochondrial biogenesis.

Because CBN was able to regulate mitochondrial ROS and Ca^{2+} levels and maintain mitochondrial bioenergetics, we then asked whether these effects of CBN are correlated to mitochondrial biogenesis. To assess the overall mitochondrial content in the HT22 cells, the MitoTracker assay was used. MitoTracker fluorescent probes are cell-permeant mitochondrionselective dyes that contain a chloromethyl moiety that covalently reacts with thiols on proteins/peptides in actively respiring mitochondria. Thus, the relative fluorescence intensity of MitoTracker in the treated cells is proportional to their corresponding mitochondrial mass in a given condition. Live-cell imaging of HT22 cells (Figure 6A–B) showed that the MitoTracker dye accumulated in the CBN-treated cells with a higher intensity of fluorescence than in the control cells, while the number of cells visualized by the Hoechst nuclear staining were similar between the two groups. Quantitative analysis confirmed that 5 μM CBN treatment for 16 hr significantly increased MitoTracker fluorescence by 4.9% in HT22 cells in comparison to the control group (Figure 6E), indicating an increase in mitochondrial mass. In contrast, treatment with 50 nM RSL3 (Figure 6C) not only reduced the cell viability but also the mitochondrial content. As visualized by fluorescence microscopy along with quantitative measurements, the MitoTracker intensity of RSL3-treated cells was significantly decreased by 8.4% relative to that of the control cells (Figure 6E). CBN was able to preserve the mitochondrial mass at the control level against RSL3-induced oxytosis/ferroptosis (Figure 6D–E). To further confirm this observation, we measured the expression level of the voltage dependent anion channel (VDAC) that is commonly used as a mitochondrial marker. Western blotting showed that VDAC was upregulated upon CBN treatment but substantially downregulated by RSL3 ($p < 0.0001$), and that this decrease was prevented by CBN ($p < 0.0001$) (Figure 6F). These results suggested that CBN and RSL3 might alter mitochondrial biogenesis.

Mitochondrial biogenesis is tightly regulated by AMP-activated protein kinase (AMPK), sirtuin-1 (SIRT1), and peroxisome proliferator-activated receptor- γ coactivator 1α (PGC-1α) [56, 57]. Hence, we examined the AMPK/SIRT1/PGC-1α pathway and measured the protein levels of AMPK, SIRT1, PGC-1α, as well as their downstream effectors nuclear respiratory factor 1 (NRF1) and mitochondrial transcription factor A (TFAM) in HT22 cells. Western blotting (Figure 6G–H) showed that CBN upregulated the protein expression of SIRT1, pAMPK(Thr172)/AMPK, and NRF1, while there were no apparent effects on PGC-1α and TFAM levels. However, the levels of all of these proteins were downregulated significantly upon RSL3 treatment and the decrease was prevented by CBN. Thus, these immunoblotting data are in agreement with the MitoTracker assay, demonstrating that CBN activated mitochondrial biogenesis which was decreased by RSL3 treatment.

CBN regulates mitochondrial dynamics.

Mitochondria form a dynamic network with the ability to constantly elongate (fusion) and fragment (fission) within cells. In coordination with mitochondrial bioenergetics and biogenesis, mitochondrial fusion/fission dynamics play a crucial role in mitochondrial quality control and resilience against cellular stresses [58]. Although oxytosis/ferroptosis represents a regulated cell death pathway that involves mitochondrial oxidative stress and ROS production and has been shown to induce changes in mitochondrial morphology [47], it has not been mechanistically examined whether oxytosis/ferroptosis causes defects in mitochondrial dynamics and if CBN can sustain a healthy balance of mitochondrial fusion and fission.

To examine the delicate changes in mitochondrial morphology in response to different treatment conditions, we generated a HT22 mt-GFP cell line with GFP-labeled mitochondria. Following the desired treatments, the cells were fixed and subjected to Airyscan super-resolution confocal microscopy analyses. As visualized in Figure 7A, the control HT22 cells contained tubular-shaped, elongated, and branched networks of mitochondria as previously reported [59]. The cells treated with 5 μM CBN for 16 hr (Figure 7B) appeared to have more widespread mitochondria with highly branched networks. In contrast, the cells treated with 50 nM RSL3 for 16 hr showed a large number of fragmented, shortened and globular/donut-shaped mitochondria (Figure 7C), similar to what has been seen in stressed, pathologic, or aging/senescent neurons [60, 61]. Pretreatment of CBN for 1 hr followed by RSL3 co-incubation for 16 hr was able to reduce the number of fragmented mitochondria and maintain the tubular mitochondrial morphology and networks similar to the control cells (Figure 7D).

Quantitative image analyses of the mitochondrial morphology further supported the effects of CBN and RSL3 on mitochondrial dynamics. The mitochondrial network parameters were scored and analyzed statistically. Exposure of HT22 cells to CBN at 5 μM significantly increased the individual and summed branch lengths of mitochondria (Figure 7F–G), while there were no apparent effects on the mitochondrial footprints (Figure 7E) and network branches (Figure 7H). The results suggested an increase of mitochondrial fusion with CBN treatment. However, following exposure to 50 nM RSL3, HT22 cells showed a significant reduction in their mitochondrial footprints, mitochondrial branch lengths and

network branches (Figure 7E–H). This indicated a substantial fragmentation of mitochondria from large networks into small structures associated with mitochondrial fission. Treatment with CBN was able to prevent the mitochondrial fragmentation induced by RSL3 and the mitochondrial network features were improved to control levels (Figure 7E–H).

We next measured by Western blotting the protein levels of mitochondrial fusion proteins including optic atrophy protein 1 (OPA1) and mitofusin 2 (MFN2), as well as mitochondrial fission proteins including dynamin-related protein 1 (DRP1) and mitochondrial fission factor (MFF) in HT22 cells. As shown in Figure 7I, K, OPA1 and MFN2 were upregulated upon CBN treatment for 16 hr. In contrast, the cells treated with RSL3 significantly downregulated OPA1 while MFN2 was unaffected. Co-treatment with CBN and RSL3 enhanced the expression of OPA1 but not MFN2. Regarding the mitochondrial fission proteins, CBN significantly enhanced the expression of MFF but not DRP1, while RSL3 decreased the expression levels of both DRP1 and MFF in HT22 cells (Figure 7J, K). Co-treatment with CBN and RSL3 restored DRP1 levels but not MFF levels. Overall, the super-resolution microscopy and immunoblotting data suggest that CBN is an effective modulator of mitochondrial dynamics against oxytosis/ferroptosis.

CBN requires functional mitochondria to protect against oxytosis/ferroptosis.

Given the multiple effects of CBN on mitochondria, we determined if mitochondria play an essential role in the protective effects of CBN against oxytosis/ferroptosis. To do this, we generated a HT22 mt-GFP/mCherry-Parkin cell line, which overexpresses the ubiquitin E3 ligase Parkin protein in addition to the GFP-labeled mitochondria. As characterized previously [27, 42], overexpression of Parkin coupled with treatment with mitochondrial uncouplers (e.g., FCCP) activates mitophagy and thus can be used to experimentally eliminate mitochondria partially or completely. Using the HT22 mt-GFP/mCherry-Parkin cells and mt-GFP cells as a wildtype (WT) control, we asked whether the protective effects of CBN against oxytosis/ferroptosis persisted after mitochondrial clearance.

We analyzed the differential cellular phenotypes under eight treatment conditions with the mt-GFP WT or mt-GFP/mCherry-Parkin cells treated with vehicle, CBN, RSL3, CBN+RSL3, FCCP, FCCP+CBN, FCCP+RSL3, and FCCP+CBN+RSL3, respectively. To determine if CBN offered similar protection in the two cell lines in the presence of mitochondria, the mt-GFP WT or mt-GFP/mCherry-Parkin cells seeded at the same density were treated with vehicle, CBN, RSL3, or CBN+RSL3 for 16 hr. Fluorescence microscopic images (Figure 8A) illustrate that CBN exhibited strong and equivalent protection against RSL3-induced cell death in both cell lines. When both were pretreated with FCCP (5 μM) for 24 hr (Figure 8B), the mt-GFP/mCherry-Parkin cells showed a partial removal of mitochondria as evidenced by fewer and compressed/clustered GFP-labeled mitochondria mostly surrounding the nucleus, indicative of widespread mitophagy. Western blotting confirmed a substantial reduction in the expression of mitochondrial markers (i.e., VDAC, TOM20) in the HT22 mt-GFP/mCherry-Parkin cells after FCCP treatment for 24 hr (Supplementary Materials Figure S4). In contrast, FCCP did not induce mitochondrial loss in the mt-GFP WT cells as the GFP-labeled mitochondria were extensively distributed in the soma and their mitochondrial markers were well retained (Figure 8B and S4). As shown

in Figure 8B, CBN treatment did not alter the FCCP-induced loss of mitochondria in the mt-GFP/mCherry-Parkin cells. After FCCP treatment, both cell lines still responded to RSL3 treatment becoming rounded, shrinking and undergoing the typical oxytotic/ferroptotic cell death process. Importantly, while CBN protected the mt-GFP WT cells from RSL3, it failed to protect the mt-GFP/mCherry-Parkin cells from oxytosis/ferroptosis (Figure 8B, bottom row of panel).

In addition to fluorescence microscopy, quantitative cell viability assessments on both cell lines following the different treatment conditions were performed. To account for mitochondrial depletion, instead of using the MTT assay that depends on mitochondrial metabolism, a DNA-based cell proliferation assay was used. In concordance with the microscopic observations, CBN had similar protective effects against RSL3 in both the mt-GFP WT and mt-GFP/mCherryParkin cells when they were not pretreated with FCCP (Figure 8C–D). Both cell lines showed a decreased cell number in response to FCCP treatment after 40 hr (about 40% decrease in cell viability compared to the vehicle control), which could be due to the uncoupling effect of FCCP on the ETC and consequent decreases in ATP production required for cell proliferation. After FCCP pretreatment for 24 hr, co-treatment with CBN of both cell cultures for an additional 16 hr did not further change the cell numbers. RSL3 induced a dramatic decrease in cell viability down to approximately 10–15% in both the FCCP pretreated mt-GFP WT and mt-GFP/mCherry-Parkin cells. In contrast, CBN treatment of RSL3-treated cells showed very different effects between the two cell lines (Figure 8C–D). While CBN was protective in the mt-GFP WT cells, it did not protect in mt-GFP/mCherry-Parkin cells with partial mitochondrial clearance.

To provide further support for the critical role of mitochondria in the protective effects of CBN against oxytosis/ferroptosis, two oxytotic/ferroptotic inhibitors, ferrostatin and MitoQ with distinct biochemical mechanisms, were also evaluated and compared to CBN in the HT22 mtGFP/mCherry-Parkin cells. Ferrostatin is a radical-trapping antioxidant that does not rely on mitochondria to inhibit oxytosis/ferroptosis [43], and as mentioned above it showed a potent anti-lipid autoxidation effect different from CBN in the cell-free, liposome-based assay (Figure 3D). By contrast, MitoQ is a selective mitochondrially-targeted antioxidant [32, 62]. As shown in Figure 8E, without FCCP pretreatment the three compounds effectively protected from RSL3-induced cell death. However, in the FCCP-mediated mitochondria-depleted cells, only ferrostatin rescued the cells from RSL3 treatment, whereas MitoQ showed no cytoprotection, similarly to CBN. Together, these results establish that the protective effects of CBN against oxytosis/ferroptosis physically require functional mitochondria.

Discussion

An increasing number of studies have shown that phytocannabinoids possess a broad range of pharmacological profiles through the modulation of non-canonical elements and biological pathways aside from the canonical targets such as cannabinoid CB1/CB2 receptors and endocannabinoid enzymes. They are promising drug candidates to combat excitotoxicity, oxidative stress, neuroinflammation, and protein aggregation in the central nervous system (CNS) [63]. CBN is a minor phytocannabinoid derived from oxidative

degradation of THC, mostly found in aged *Cannabis* [64]. CBN is a weak agonist of CB1/CB2 receptors with 10 to 100-fold lower binding affinities compared to THC and the affinity is tissue- or cell-type specific [65, 66]. Thus, CBN is generally considered as a non-psychoactive phytocannabinoid and is not listed as a Schedule I controlled substance by the U.S. Drug Enforcement Administration (USDEA) nor in the Schedules of the United Nations International Drug Control Conventions [67]. *In silico* physicochemical prediction (Figure 1) indicates that CBN has a relatively good profile of CNS druglike properties that obeys the Lipinski's rule of five [68]. Owing to the presence of an additional aromatic ring as compared to THC, CBN is metabolically more stable and its bioavailability after oral or inhaled administration has been reported in the range of 10 to 40% [69]. Preclinical and limited clinical evaluations have also shown that CBN has good brain penetrance with excellent safety and pharmacokinetic profiles in animals and humans [70–75]. However, pharmacological and mechanistic studies on CBN as a treatment for age-associated neurodegenerative diseases have not been reported. In the present study, we demonstrated that CBN effectively protected from both glutamate and RSL3-induced oxytosis/ferroptosis (Figure 2) and it has a large safety margin and low cytotoxicity across different cell types.

Oxytosis/ferroptosis recapitulates several aspects of mitochondrial pathology that are relevant to neurodegenerative diseases [6, 41]. Specifically, mitochondrial oxidative stress is a major pathological hallmark of neurodegenerative disorders including AD, PD, and HD [2, 76, 77]. As shown in Figure 3, CBN potently prevented both cellular and mitochondrial ROS production induced by oxytosis/ferroptosis. Although CBN effectively inhibited cellular lipid peroxidation, its action against cell-free lipid autoxidation was negligible. Given that lipid peroxidation is generally considered as an executive step leading to the disruption of cellular membrane integrity downstream in the oxytosis/ferroptosis pathway, the discrepancy between the cell-based and cell-free assays suggests that CBN does not directly inhibit RSL3-induced lipid peroxidation. This idea is supported by the results of the cell-free TEAC and iron binding assays which indicate that CBN, albeit its strong cytoprotection at relevant doses (5 to 10 μM), is neither an effective free radical scavenger nor an iron chelator. In addition, CBN showed no impact on the total cellular GSH levels regardless of RSL3 co-treatment. Because RSL3 directly inhibits GPX4, an enzyme that is dependent on GSH, it is likely that CBN acts on targets downstream of GSH synthesis but upstream of lipid peroxidation in the oxytosis/ferroptosis pathway.

Immunoblotting demonstrated that CBN was able to activate the antioxidant defense system via the upregulation of Nrf2, HO-1, SOD2 and GPX4 in HT22 cells. While no effect on cellular GSH synthesis was seen, CBN appears to promote a plethora of other endogenous antioxidant mediators that could reduce/neutralize ROS and lipid peroxides against oxidative injury [78, 79]. In parallel, we found a strong increase in the mitochondrial chaperone HSP60 by RSL3 in response to mitochondrial oxidative stress that was effectively prevented by CBN, suggesting that CBN might be specifically acting on mitochondria to prevent stress. To address this question, we examined the effects of CBN on central aspects of mitochondrial function both alone and in the presence of RSL3.

Numerous studies have shown that prolonged mitochondrial Ca^{2+} overload leads to increased ROS generation, bioenergetic and metabolic disturbance, and induction of cell death associated with mitochondrial oxidative stress [49]. RSL3 increased mitochondrial Ca^{2+} which was inhibited by CBN possibly, at least in part, via the downregulation of MCU (Figure 4). Owing to the pathophysiological relevance of MCU in neurodegenerative diseases and its role in Ca^{2+}-dependent mitochondrial bioenergetics [50, 51], the effects of CBN on Ca^{2+} regulation could be a beneficial feature for neurotherapies.

Furthermore, we demonstrated that CBN directly modulated mitochondrial bioenergetics against oxytosis/ferroptosis (Figure 5). Consistent with recent reports on RSL3-mediated bioenergetic impairments in mouse embryonic fibroblasts (MEF) and hepatocellular carcinoma (HCC) [47, 80], the real-time mitochondrial metabolic analysis clearly illustrated that RSL3 caused mitochondrial dysfunction at least partly by decreasing electron flow through the ETC, resulting in a reduction in mitochondrial respiration and cellular ATP production in both cannabinoid receptor-deficient (i.e., HT22 cells) and cannabinoid receptor-expressing cells (i.e., embryonic cortical neurons). CBN maintained the bioenergetic phenotype against the damaging effects of RSL3 and showed comparable respiratory profiles in both cell types. These results support the idea that at least part of the neuroprotective effects of CBN against oxytosis/ferroptosis could be due to the maintenance of mitochondrial bioenergetics regardless of the presence of cannabinoid receptors in the cells.

Since the generation of mtROS mainly takes place at the ETC during OXPHOS, particularly at complexes I, II and III [81, 82], the upregulation of OXPHOS complexes induced by RSL3 is plausibly a compensatory response to the decrease in ETC activity, and this also correlated well with the significant accumulation of mtROS in the cells (Figure 3). This aberrant mtROS production could then further impair the OXPHOS process for mitochondrial respiration providing a feed forward loop which promotes cell death. By contrast, CBN counteracted these effects on mitochondria. Intriguingly, short-term treatment with CBN depolarized $\Delta\Psi m$ in HT22 cells, whose effect was analogous to that of the mitochondrial uncoupler FCCP and was not affected by RSL3 treatment (Figure 5E). Our data are consistent with previous reports [54, 82] which showed that transient or modest depolarization of mitochondrial membranes (e.g., using mitochondrial uncouplers) could diminish mtROS production and mitochondrial respiration. Thus, CBN shows a direct effect on mitochondria and might subtly modulate $\Delta\Psi m$ for neuroprotection through a similar mechanism. Moreover, because of its high lipophilicity (cLogP = 7.4, TPSA = 29) (Figure 1), CBN could possibly diffuse or anchor onto mitochondrial membranes to alter the membrane fluidity which has been shown to affect the efficiency of mitochondrial respiration [83, 84]. Overall, the data support the idea that CBN can prevent the toxic effects of RSL3 through suppressing mtROS and Ca^{2+} uptake, depolarizing $\Delta\Psi m$, downregulating the increase in the OXPHOS complexes, and eventually preserving mitochondrial bioenergetics in the cells.

Besides mitochondrial oxidative stress and bioenergetics, the impact of RSL3 on mitochondrial biogenesis and fusion/fission dynamics offers new insights into the effects of oxytosis/ferroptosis on mitochondrial function beyond the classical markers of redox

biology. We showed that RSL3 induces the dysregulation of mitochondrial biogenesis plausibly through interfering with the AMPK/SIRT1/PGC-1α pathway [56, 57], whereas CBN conferred a beneficial effect by stimulating mitochondrial biogenesis against RSL3 (Figure 6). Additionally, extending the phenotypic observations by Jelinek et al. [47], our study found that mitochondrial fragmentation occurred in response to RSL3 treatment, indicating an imbalance in dynamics towards fission. CBN was able to restore this fusion/fission balance (Figure 7). Changes in mitochondrial morphology have been implicated in the modulation of bioenergetics, OXPHOS efficiency, and quality control in mitochondria in response to cellular stresses, insults, or the aging process [60, 61]. Particularly, elongated mitochondria have been shown to restore mitochondrial respiration and ATP production as well as redistribute biomaterials to rescue defective mitochondria [58, 85], all of which were indeed found to be modulated by CBN (Figure 5). Because CBN promoted biogenesis to generate new and healthy mitochondria to fuel mitochondrial fusion, this could potentially stimulate the upregulation of mitochondrial fusion proteins like OPA1 and MFN2. On the other hand, CBN facilitated the fission process to remove damaged mitochondria possibly via intervening in the AMPK/MFF/DRP1 pathway [86]. Overall, it appears that CBN exerts its mitochondrially protective effects at least partly by promoting mitochondrial biogenesis, restoring mitochondrial fusion, and sustaining mitochondrial bioenergetics in the cells (Figure 5–7).

Finally, the results obtained from an inducible, mitochondrially-depleted cell line (Figure 8) along with the ΔΨm assay (Figure 5E) reinforce the idea that CBN inhibits oxytosis/ferroptosis through directly targeting mitochondria and that its neuroprotective effects rely on functional mitochondria in the cells. These novel observations also indicate that while GPX4-dependent oxytosis/ferroptosis induced by RSL3 does not require mitochondria to initiate cell death, the maintenance of healthy mitochondria can still provide cytoprotection. Therefore, these results suggest that targeting mitochondria in general against age-related insults, regardless of the direct/indirect impact of these insults on mitochondria, is a promising therapeutic strategy for age-associated neurodegenerative diseases [6].

Conclusions

In this study, we systematically examined key aspects of mitochondrial physiology to determine the mechanism of action underlying the neuroprotective effects of CBN against oxytosis/ferroptosis. In this comprehensive investigation, we identified the critical role of mitochondria in CBN-mediated protection against the oxytosis/ferroptosis pathway by examining the interplay between oxidative stress, Ca^{2+} uptake, membrane potential, bioenergetics, biogenesis, and fusion/fission dynamics (Figure 9). To the best of our knowledge, this is the first report using a mitochondrially-depleted cell line as a novel approach to demonstrate that functional mitochondria are pivotal for the protection against oxytosis/ferroptosis mediated by a small molecule. In the future, this technique could prove very useful for the identification of other mitochondrially-targeted compounds. Additionally, the new findings uncover that CBN maintains mitochondrial homeostasis against oxytosis/ferroptosis, even when the initiation of cell death does not appear to require mitochondria. It effectively reduces mitochondrial oxidative stress in terms of mtROS and lipid peroxidation and prevents mitochondrial Ca^{2+} dysregulation. These effects of CBN

are at least in part involved in the activation of endogenous antioxidant defenses and the downregulation of MCU. Moreover, CBN directly targets mitochondria to modulate ΔΨm and the OXPHOS complexes, resulting in the restoration of mitochondrial bioenergetics as well as the regulation of mitochondrial biogenesis and dynamics via AMPK signaling to improve mitochondrial health.

Given the biological importance and therapeutic relevance of mitochondrial dysfunction in many age-associated neurodegenerative diseases, an in-depth understanding of the root causes and mechanistic links between oxytosis/ferroptosis and mitochondrial pathophysiology in terms of signal transduction, metabolic pathways, and cellular phenotypes warrants further investigation. Most importantly, our study offers strong evidence that non-psychoactive phytocannabinoids such as CBN can elicit neuroprotective actions independent of the canonical CB1/CB2 pathway and that they could serve as valuable CNS drug leads. Future efforts on target identification, structure-activity relationship driven lead optimization to improve oral bioavailability, CNS druglikeness, and pharmacokinetic parameters, as well as *in vivo* efficacy studies in animal models should pave the way for the development of new drug candidates derived from CBN or other non-psychoactive cannabinoids to treat age-associated neurodegenerative diseases.

Supplementary Material

Refer to Web version on PubMed Central for supplementary material.

Acknowledgments

The research was conducted under a US-DEA license. The work was supported by the Paul F. Glenn Center for Biology of Aging Research at the Salk Institute Fellowship (ZL), a Shiley Foundation Fellowship (DS-C), a Bundy Foundation Fellowship (DK), the Shiley-Marcos Alzheimer's Disease Research Center at the University of California, San Diego (AC), an Innovation Award from the Salk Institute (AC), and the National Institutes of Health grants R01AG069206, RF1AG054714 and R21AG064287 (PM and DS). We thank the Waitt Advanced Biophotonics Core Facility, the Stem Cell Core Facility, the Next Generation Sequencing Core Facility, and the Mass Spectrometry Core Facility of the Salk Institute with funding from the NIH-NCI CCSG grant P30014195, an NIH S10 award for metabolic instrumentation S10OD021815, the Waitt Foundation, the Chapman Foundation, the Helmsley Charitable Trust, and the Helmsley Center for Genomic Medicine for technical support with data acquisition. NMR spectra were collected at the UCSD Skaggs School of Pharmacy and Pharmaceutical Sciences NMR Facility.

Abbreviations:

AD	Alzheimer's disease
PD	Parkinson's disease
HD	Huntington's disease
CNS	central nervous system
mt	mitochondria
DNA	deoxyribonucleic acid
ETC	electron transport chain

OXPHOS	oxidative phosphorylation
ROS	reactive oxygen species
ΔΨm	mitochondrial membrane potential
PGC-1α	peroxisome proliferator-activated receptor- γ coactivator 1α
AMPK	adenosine monophosphate-activated protein kinase
SIRT1	sirtuin-1
NRF1	nuclear respiratory factor 1
TFAM	mitochondrial transcription factor A
OPA1	optic atrophy protein 1
MFN2	mitofusin 2
DRP1	dynamin-related protein 1
MFF	mitochondrial fission factor
Nrf2	nuclear erythroid 2-related factor
ATF4	activating transcription factor 4
HO-1	heme oxygenase-1
SOD2	superoxide dismutase 2
HSP60	mitochondrial chaperone heat shock protein 60
Xc-	cystine/glutamate antiporter
GSH	glutathione
GPX4	glutathione peroxidase 4
VDAC	voltage-dependent anion channel
TOM20	translocase of the outer membrane subunit 20
MCU	mitochondrial calcium uniporter
GFP	green fluorescent protein
CB1/CB2	cannabinoid receptors 1 and 2
NADPH	nicotinamide adenine dinucleotide phosphate
ATP	adenosine triphosphate
OCR	oxygen consumption rate
TEAC	Trolox equivalent antioxidant capacity

WT	wildtype
qPCR	quantitative polymerase chain reaction
NMR	nuclear magnetic resonance
HR-MS	high-resolution mass spectrometry
CBN	cannabinol
THC	tetrahydrocannabinol
CBD	cannabidiol
ABTS	2,2'-azino-bis(3-ethylbenzothiazoline-6-sulfonic acid)
FCCP	carbonyl cyanide-4-(trifluoromethoxy)phenylhydrazone
MTT	3-(4,5-dimethylthiazol-2-yl)-2,5-diphenyltetrazolium bromide
EC_{50}	half maximal effective concentration.

References

[1]. Hou Y, Dan X, Babbar M, Wei Y, Hasselbalch SG, Croteau DL, Bohr VA, Ageing as a risk factor for neurodegenerative disease, Nat. Rev. Neurol 15(10) (2019) 565–581. [PubMed: 31501588]

[2]. Butterfield DA, Halliwell B, Oxidative stress, dysfunctional glucose metabolism and Alzheimer disease, Nat. Rev. Neurosci 20(3) (2019) 148–160. [PubMed: 30737462]

[3]. Nunnari J, Suomalainen A, Mitochondria: in sickness and in health, Cell 148(6) (2012) 1145–1159. [PubMed: 22424226]

[4]. Lin MT, Beal MF, Mitochondrial dysfunction and oxidative stress in neurodegenerative diseases, Nature 443(7113) (2006) 787–795. [PubMed: 17051205]

[5]. Schubert D, Currais A, Goldberg J, Finley K, Petrascheck M, Maher P, Geroneuroprotectors: effective geroprotectors for the brain, Trends Pharmacol. Sci 39(12) (2018) 1004–1007. [PubMed: 30446211]

[6]. Liang Z, Currais A, Soriano-Castell D, Schubert D, Maher P, Natural products targeting mitochondria: emerging therapeutics for age-associated neurological disorders, Pharmacol. Ther 221 (2021) 107749. [PubMed: 33227325]

[7]. Hara Y, McKeehan N, Fillit HM, Translating the biology of aging into novel therapeutics for Alzheimer disease, Neurology 92(2) (2019) 84–93. [PubMed: 30530798]

[8]. Tan S, Schubert D, Maher P, Oxytosis: a novel form of programmed cell death, Curr. Top. Med. Chem 1(6) (2001) 497–506. [PubMed: 11895126]

[9]. Maher P, Currais A, Schubert D, Using the oxytosis/ferroptosis pathway to understand and treat age-associated neurodegenerative diseases, Cell Chem. Biol 27(12) (2020) 1456–1471. [PubMed: 33176157]

[10]. Dixon Scott J., Lemberg Kathryn M., Lamprecht Michael R., Skouta R, Zaitsev Eleina M., Gleason Caroline E., Patel Darpan N., Bauer Andras J., Cantley Alexandra M., Yang Wan S., Morrison B, Stockwell Brent R., Ferroptosis: an iron-dependent form of nonapoptotic cell death, Cell 149(5) (2012) 1060–1072. [PubMed: 22632970]

[11]. Soriano-Castell D, Liang Z, Maher P, Currais A, The search for anti-oxytotic/ferroptotic compounds in the plant world, Br. J. Pharmacol 178(18) (2021) 3611–3626. [PubMed: 33931859]

[12]. Abel EL, Marihuana, the first twelve thousand years, 1st ed., Springer1980.

[13]. Ren M, Tang Z, Wu X, Spengler R, Jiang H, Yang Y, Boivin N, The origins of cannabis smoking: chemical residue evidence from the first millennium BCE in the Pamirs, Sci. Adv 5(6) (2019) eaaw1391. [PubMed: 31206023]

[14]. Fernández-Ruiz J, The biomedical challenge of neurodegenerative disorders: an opportunity for cannabinoid-based therapies to improve on the poor current therapeutic outcomes, Br. J. Pharmacol 176(10) (2019) 1370–1383. [PubMed: 29856067]

[15]. Mechoulam R, Hanuš LO, Pertwee R, Howlett AC, Early phytocannabinoid chemistry to endocannabinoids and beyond, Nat. Rev. Neurosci 15(11) (2014) 757–764. [PubMed: 25315390]

[16]. Vacek J, Vostalova J, Papouskova B, Skarupova D, Kos M, Kabelac M, Storch J, Antioxidant function of phytocannabinoids: molecular basis of their stability and cytoprotective properties under UV-irradiation, Free Radic. Biol. Med 164 (2021) 258–270. [PubMed: 33453360]

[17]. Lucas CJ, Galettis P, Schneider J, The pharmacokinetics and the pharmacodynamics of cannabinoids, Br. J. Clin. Pharmacol 84(11) (2018) 2477–2482. [PubMed: 30001569]

[18]. Schlag AK, O'Sullivan SE, Zafar RR, Nutt DJ, Current controversies in medical cannabis: recent developments in human clinical applications and potential therapeutics, Neuropharmacology 191 (2021) 108586. [PubMed: 33940011]

[19]. Izzo AA, Borrelli F, Capasso R, Di Marzo V, Mechoulam R, Non-psychotropic plant cannabinoids: new therapeutic opportunities from an ancient herb, Trends Pharmacol. Sci 30(10) (2009) 515–527. [PubMed: 19729208]

[20]. Stone NL, Murphy AJ, England TJ, O'Sullivan SE, A systematic review of minor phytocannabinoids with promising neuroprotective potential, Br. J. Pharmacol 177(19) (2020) 4330–4352. [PubMed: 32608035]

[21]. Wilkinson ST, Yarnell S, Radhakrishnan R, Ball SA, D'Souza DC, Marijuana legalization: impact on physicians and public health, Annu. Rev. Med 67(1) (2016) 453–466. [PubMed: 26515984]

[22]. Schubert D, Kepchia D, Liang Z, Dargusch R, Goldberg J, Maher P, Efficacy of cannabinoids in a pre-clinical drug-screening platform for Alzheimer's disease, Mol. Neurobiol 56(11) (2019) 7719–7730. [PubMed: 31104297]

[23]. Currais A, Quehenberger O, M Armando A, Daugherty D, Maher P, Schubert D, Amyloid proteotoxicity initiates an inflammatory response blocked by cannabinoids, npj Aging Mech. Dis 2 (2016) 16012. [PubMed: 28721267]

[24]. Kupče E, Freeman R, Fast multidimensional NMR by polarization sharing, Magn. Reson. Chem 45(1) (2007) 2–4. [PubMed: 17125135]

[25]. Caprioglio D, Mattoteia D, Minassi A, Pollastro F, Lopatriello A, Muñoz E, Taglialatela-Scafati O, Appendino G, One-pot total synthesis of cannabinol via iodine-mediated deconstructive annulation, Org. Lett 21(15) (2019) 6122–6125. [PubMed: 31339327]

[26]. Li Y, Maher P, Schubert D, A role for 12-lipoxygenase in nerve cell death caused by glutathione depletion, Neuron 19(2) (1997) 453–463. [PubMed: 9292733]

[27]. Correia-Melo C, Ichim G, Tait SWG, Passos JF, Depletion of mitochondria in mammalian cells through enforced mitophagy, Nat. Protoc 12(1) (2017) 183–194. [PubMed: 28005069]

[28]. Liang Z, Zhang B, Su WW, Williams PG, Li QX, C-Glycosylflavones alleviate tau phosphorylation and amyloid neurotoxicity through GSK3β inhibition, ACS Chem. Neurosci 7(7) (2016) 912–923. [PubMed: 27213824]

[29]. Fischer W, Currais A, Liang Z, Pinto A, Maher P, Old age-associated phenotypic screening for Alzheimer's disease drug candidates identifies sterubin as a potent neuroprotective compound from Yerba santa, Redox Biol. 21 (2019) 101089. [PubMed: 30594901]

[30]. Huang L, McClatchy DB, Maher P, Liang Z, Diedrich JK, Soriano-Castell D, Goldberg J, Shokhirev M, Yates JR, Schubert D, Currais A, Intracellular amyloid toxicity induces oxytosis/ferroptosis regulated cell death, Cell Death Dis. 11(10) (2020) 828. [PubMed: 33024077]

[31]. Drummen GPC, van Liebergen LCM, Op den Kamp JAF, Post JA, C11BODIPY581/591, an oxidation-sensitive fluorescent lipid peroxidation probe: (micro)spectroscopic characterization and validation of methodology, Free Radic. Biol. Med 33(4) (2002) 473–490. [PubMed: 12160930]

[32]. Soriano-Castell D, Currais A, Maher P, Defining a pharmacological inhibitor fingerprint for oxytosis/ferroptosis, Free Radic. Biol. Med 171 (2021) 219–231. [PubMed: 34010663]

[33]. Re R, Pellegrini N, Proteggente A, Pannala A, Yang M, Rice-Evans C, Antioxidant activity applying an improved ABTS radical cation decolorization assay, Free Radic. Biol. Med 26(9) (1999) 1231–1237. [PubMed: 10381194]

[34]. Soriano-Castell D, Liang Z, Maher P, Currais A, Profiling the chemical nature of anti-oxytotic/ferroptotic compounds with phenotypic screening, Free Radic. Biol. Med 177 (2021) 313–325. [PubMed: 34748909]

[35]. Goldberg J, Currais A, Ates G, Huang L, Shokhirev M, Maher P, Schubert D, Targeting of intracellular Ca2+ stores as a therapeutic strategy against age-related neurotoxicities, npj Aging Mech. Dis 6(1) (2020) 10. [PubMed: 32884834]

[36]. Liang Z, Zhang B, Xu M, Morisseau C, Hwang SH, Hammock BD, Li QX, 1Trifluoromethoxyphenyl-3-(1-propionylpiperidin-4-yl) urea, a selective and potent dual inhibitor of soluble epoxide hydrolase and p38 kinase intervenes in Alzheimer's signaling in human nerve cells, ACS Chem. Neurosci 10(9) (2019) 4018–4030. [PubMed: 31378059]

[37]. Ay M, Luo J, Langley M, Jin H, Anantharam V, Kanthasamy A, Kanthasamy AG, Molecular mechanisms underlying protective effects of quercetin against mitochondrial dysfunction and progressive dopaminergic neurodegeneration in cell culture and MitoPark transgenic mouse models of Parkinson's disease, J. Neurochem 141(5) (2017) 766–782. [PubMed: 28376279]

[38]. Valente AJ, Maddalena LA, Robb EL, Moradi F, Stuart JA, A simple ImageJ macro tool for analyzing mitochondrial network morphology in mammalian cell culture, Acta Histochem. 119(3) (2017) 315–326. [PubMed: 28314612]

[39]. Teske JA, Deiters A, A cyclotrimerization route to cannabinoids, Org. Lett 10(11) (2008) 2195–2198. [PubMed: 18452299]

[40]. Marsicano G, Moosmann B, Hermann H, Lutz B, Behl C, Neuroprotective properties of cannabinoids against oxidative stress: role of the cannabinoid receptor CB1, J. Neurochem 80(3) (2002) 448–456. [PubMed: 11905991]

[41]. Lewerenz J, Ates G, Methner A, Conrad M, Maher P, Oxytosis/ferroptosis—(Re-) emerging roles for oxidative stress-dependent non-apoptotic cell death in diseases of the central nervous system, Front. Neurosci 12 (2018) 214. [PubMed: 29731704]

[42]. Gao M, Yi J, Zhu J, Minikes AM, Monian P, Thompson CB, Jiang X, Role of mitochondria in ferroptosis, Mol. Cell 73(2) (2019) 354–363.e3. [PubMed: 30581146]

[43]. Zilka O, Shah R, Li B, Friedmann Angeli JP, Griesser M, Conrad M, Pratt DA, On the mechanism of cytoprotection by ferrostatin-1 and liproxstatin-1 and the role of lipid peroxidation in ferroptotic cell death, ACS Cent. Sci 3(3) (2017) 232–243. [PubMed: 28386601]

[44]. Stockwell BR, Friedmann Angeli JP, Bayir H, Bush AI, Conrad M, Dixon SJ, Fulda S, Gascón S, Hatzios SK, Kagan VE, Noel K, Jiang X, Linkermann A, Murphy ME, Overholtzer M, Oyagi A, Pagnussat GC, Park J, Ran Q, Rosenfeld CS, Salnikow K, Tang D, Torti FM, Torti SV, Toyokuni S, Woerpel KA, Zhang DD, Ferroptosis: a regulated cell death nexus linking metabolism, redox biology, and disease, Cell 171(2) (2017) 273–285. [PubMed: 28985560]

[45]. Song JH, Lee H-J, Kang KS, Procyanidin C1 activates the Nrf2/HO-1 signaling pathway to prevent glutamate-induced apoptotic HT22 cell death, Int. J. Mol. Sci 20(1) (2019) 142.

[46]. Cox CS, McKay SE, Holmbeck MA, Christian BE, Scortea AC, Tsay AJ, Newman LE, Shadel GS, Mitohormesis in mice via sustained basal activation of mitochondrial and antioxidant signaling, Cell Metab. 28(5) (2018) 776–786.e5. [PubMed: 30122556]

[47]. Jelinek A, Heyder L, Daude M, Plessner M, Krippner S, Grosse R, Diederich WE, Culmsee C, Mitochondrial rescue prevents glutathione peroxidase-dependent ferroptosis, Free Radic. Biol. Med 117 (2018) 45–57. [PubMed: 29378335]

[48]. Peter B, Raffaella M, Anne Sigaard B, Molecular chaperone disorders: defective Hsp60 in neurodegeneration, Curr. Top. Med. Chem 12(22) (2012) 2491–2503. [PubMed: 23339303]

[49]. Calvo-Rodriguez M, Bacskai BJ, Mitochondria and calcium in Alzheimer's disease: from cell signaling to neuronal cell death, Trends Neurosci. 44(2) (2021) 136–151. [PubMed: 33160650]

[50]. Tomar D, Dong Z, Shanmughapriya S, Koch Diana A., Thomas T, Hoffman Nicholas E., Timbalia Shrishiv A., Goldman Samuel J., Breves Sarah L., Corbally Daniel P., Nemani N,

Fairweather Joseph P., Cutri Allison R., Zhang X, Song J, Jaña F, Huang J, Barrero C, Rabinowitz Joseph E., Luongo Timothy S., Schumacher Sarah M., Rockman ME, Dietrich A, Merali S, Caplan J, Stathopulos P, Ahima Rexford S., Cheung Joseph Y., Houser Steven R., Koch Walter J., Patel V, Gohil Vishal M., Elrod John W., Rajan S, Madesh M, MCUR1 is a scaffold factor for the MCU complex function and promotes mitochondrial bioenergetics, Cell Rep. 15(8) (2016) 1673–1685. [PubMed: 27184846]

[51]. Pérez MJ, Ponce DP, Aranguiz A, Behrens MI, Quintanilla RA, Mitochondrial permeability transition pore contributes to mitochondrial dysfunction in fibroblasts of patients with sporadic Alzheimer's disease, Redox Biol. 19 (2018) 290–300. [PubMed: 30199818]

[52]. Cunnane SC, Trushina E, Morland C, Prigione A, Casadesus G, Andrews ZB, Beal MF, Bergersen LH, Brinton RD, de la Monte S, Eckert A, Harvey J, Jeggo R, Jhamandas JH, Kann O, la Cour CM, Martin WF, Mithieux G, Moreira PI, Murphy MP, Nave K-A, Nuriel T, Oliet SHR, Saudou F, Mattson MP, Swerdlow RH, Millan MJ, Brain energy rescue: an emerging therapeutic concept for neurodegenerative disorders of ageing, Nat. Rev. Drug Discov 19(9) (2020) 609–633. [PubMed: 32709961]

[53]. Vitalis T, Lainé J, Simon A, Roland A, Leterrier C, Lenkei Z, The type 1 cannabinoid receptor is highly expressed in embryonic cortical projection neurons and negatively regulates neurite growth in vitro, Eur. J. Neurosci 28(9) (2008) 1705–1718. [PubMed: 18973587]

[54]. Childress ES, Alexopoulos SJ, Hoehn KL, Santos WL, Small molecule mitochondrial uncouplers and their therapeutic potential, J. Med. Chem 61(11) (2018) 4641–4655. [PubMed: 29156129]

[55]. Anderson S, Bankier AT, Barrell BG, de Bruijn MHL, Coulson AR, Drouin J, Eperon IC, Nierlich DP, Roe BA, Sanger F, Schreier PH, Smith AJH, Staden R, Young IG, Sequence and organization of the human mitochondrial genome, Nature 290(5806) (1981) 457465.

[56]. Jamwal S, Blackburn JK, Elsworth JD, PPARγ/PGC1α signaling as a potential therapeutic target for mitochondrial biogenesis in neurodegenerative disorders, Pharmacol. Ther 219 (2021) 107705. [PubMed: 33039420]

[57]. Herzig S, Shaw RJ, AMPK: guardian of metabolism and mitochondrial homeostasis, Nat. Rev. Mol. Cell Biol 19(2) (2018) 121–135. [PubMed: 28974774]

[58]. Chan DC, Fusion and fission: interlinked processes critical for mitochondrial health, Annu. Rev. Genet 46(1) (2012) 265–287. [PubMed: 22934639]

[59]. Pfeiffer A, Jaeckel M, Lewerenz J, Noack R, Pouya A, Schacht T, Hoffmann C, Winter J, Schweiger S, Schäfer MKE, Methner A, Mitochondrial function and energy metabolism in neuronal HT22 cells resistant to oxidative stress, Br. J. Pharmacol 171(8) (2014) 2147–2158. [PubMed: 24319993]

[60]. Hara Y, Yuk F, Puri R, Janssen WGM, Rapp PR, Morrison JH, Presynaptic mitochondrial morphology in monkey prefrontal cortex correlates with working memory and is improved with estrogen treatment, Proc. Natl. Acad. Sci. U.S.A 111(1) (2014) 486–491. [PubMed: 24297907]

[61]. Ahmad T, Aggarwal K, Pattnaik B, Mukherjee S, Sethi T, Tiwari BK, Kumar M, Micheal A, Mabalirajan U, Ghosh B, Sinha Roy S, Agrawal A, Computational classification of mitochondrial shapes reflects stress and redox state, Cell Death Dis. 4(1) (2013) e461. [PubMed: 23328668]

[62]. McManus MJ, Murphy MP, Franklin JL, The mitochondria-targeted antioxidant MitoQ prevents loss of spatial memory retention and early neuropathology in a transgenic mouse model of Alzheimer's disease, J. Neurosci 31(44) (2011) 15703–15715. [PubMed: 22049413]

[63]. Hill AJ, Williams CM, Whalley BJ, Stephens GJ, Phytocannabinoids as novel therapeutic agents in CNS disorders, Pharmacol. Ther 133(1) (2012) 79–97. [PubMed: 21924288]

[64]. Pertwee RG, Cannabinoid pharmacology: the first 66 years, Br. J. Pharmacol 147(S1) (2006) S163–S171. [PubMed: 16402100]

[65]. Devane WA, Dysarz FA, Johnson MR, Melvin LS, Howlett AC, Determination and characterization of a cannabinoid receptor in rat brain, Mol. Pharmacol 34(5) (1988) 605–613. [PubMed: 2848184]

[66]. Felder CC, Joyce KE, Briley EM, Mansouri J, Mackie K, Blond O, Lai Y, Ma AL, Mitchell RL, Comparison of the pharmacology and signal transduction of the human cannabinoid CB1 and CB2 receptors, Mol. Pharmacol 48(3) (1995) 443–450. [PubMed: 7565624]

[67]. UNODC, International Drug Control Conventions, 2019. https://www.unodc.org/unodc/en/commissions/CND/Mandate_Functions/Mandate-andFunctions_Scheduling.html.

[68]. Lipinski CA, Lead- and drug-like compounds: the rule-of-five revolution, Drug Discov. Today Technol. 1(4) (2004) 337–341.

[69]. Huestis MA, Pharmacokinetics and metabolism of the plant cannabinoids, Δ9-tetrahydrocannibinol, cannabidiol and cannabinol, in: Pertwee RG (Ed.), Cannabinoids, Springer Berlin Heidelberg, Berlin, Heidelberg, 2005, pp. 657–690.

[70]. Weydt P, Hong S, Witting A, Möller T, Stella N, Kliot M, Cannabinol delays symptom onset in SOD1 (G93A) transgenic mice without affecting survival, Amyotroph. Lateral Scler. 6(3) (2005) 182–184.

[71]. Karler R, Cely W, Turkanis SA, The anticonvulsant activity of cannabidiol and cannabinol, Life Sci. 13(11) (1973) 1527–1531. [PubMed: 4768980]

[72]. Murphy LL, Steger RW, Smith MS, Bartke A, Effects of delta-9-tetrahydrocannabinol, cannabinol and cannabidiol, alone and in combinations, on luteinizing hormone and prolactin release and on hypothalamic neurotransmitters in the male rat, Neuroendocrinology 52(4) (1990) 316–321. [PubMed: 1979838]

[73]. Karniol IG, Shirakawa I, Takahashi RN, Knobel E, Musty RE, Effects of Δ9-tetrahydrocannabinol and cannabinol in man, Pharmacology 13(6) (1975) 502–512. [PubMed: 1221432]

[74]. Petitet F, Jeantaud B, Bertrand P, Imperato A, Cannabinoid penetration into mouse brain as determined by ex vivo binding, Eur. J. Pharmacol 374(3) (1999) 417–421. [PubMed: 10422786]

[75]. Agurell S, Halldin M, Lindgren JE, Ohlsson A, Widman M, Gillespie H, Hollister L, Pharmacokinetics and metabolism of delta 1-tetrahydrocannabinol and other cannabinoids with emphasis on man, Pharmacol. Rev 38(1) (1986) 21–43. [PubMed: 3012605]

[76]. Trist BG, Hare DJ, Double KL, Oxidative stress in the aging substantia nigra and the etiology of Parkinson's disease, Aging Cell 18(6) (2019) e13031. [PubMed: 31432604]

[77]. Fão L, Rego AC, Mitochondrial and redox-based therapeutic strategies in Huntington's disease, Antioxid. Redox Signaling 34(8) (2021) 650–673.

[78]. Forman HJ, Zhang H, Targeting oxidative stress in disease: promise and limitations of antioxidant therapy, Nat. Rev. Drug Discov 20(9) (2021) 689–709. [PubMed: 34194012]

[79]. Dodson M, Castro-Portuguez R, Zhang DD, NRF2 plays a critical role in mitigating lipid peroxidation and ferroptosis, Redox Biol. 23 (2019) 101107. [PubMed: 30692038]

[80]. Asperti M, Bellini S, Grillo E, Gryzik M, Cantamessa L, Ronca R, Maccarinelli F, Salvi A, De Petro G, Arosio P, Mitola S, Poli M, H-ferritin suppression and pronounced mitochondrial respiration make hepatocellular carcinoma cells sensitive to RSL3-induced ferroptosis, Free Radic. Biol. Med 169 (2021) 294–303. [PubMed: 33892112]

[81]. Sipos I, Tretter L, Adam-Vizi V, Quantitative relationship between inhibition of respiratory complexes and formation of reactive oxygen species in isolated nerve terminals, J. Neurochem 84(1) (2003) 112–118. [PubMed: 12485407]

[82]. Tan S, Sagara Y, Liu Y, Maher P, Schubert D, The regulation of reactive oxygen species production during programmed cell death, J. Cell Biol 141(6) (1998) 1423–1432. [PubMed: 9628898]

[83]. Budin I, de Rond T, Chen Y, Chan LJG, Petzold CJ, Keasling JD, Viscous control of cellular respiration by membrane lipid composition, Science 362(6419) (2018) 1186–1189. [PubMed: 30361388]

[84]. Hillard CJ, Harris RA, Bloom AS, Effects of the cannabinoids on physical properties of brain membranes and phospholipid vesicles: fluorescence studies, J. Pharmacol. Exp. Ther 232(3) (1985) 579–588. [PubMed: 2983062]

[85]. Mishra P, Chan DC, Metabolic regulation of mitochondrial dynamics, J. Cell Biol 212(4) (2016) 379–387. [PubMed: 26858267]

[86]. Toyama EQ, Herzig S, Courchet J, Lewis TL Jr., Losón OC, Hellberg K, Young NP, Chen H, Polleux F, Chan DC, Shaw RJ, AMP-activated protein kinase mediates mitochondrial fission in response to energy stress, Science 351(6270) (2016) 275–281. [PubMed: 26816379]

Highlights

- Maintenance of mitochondrial homeostasis protects against oxytosis/ferroptosis.
- CBN is a novel inhibitor of oxytosis/ferroptosis directly targeting mitochondria.
- CBN maintains key parameters of mitochondrial function for neuroprotection.
- CBN protects nerve cells independently of cannabinoid receptors.
- CBN activates endogenous antioxidant defenses and AMPK signaling.

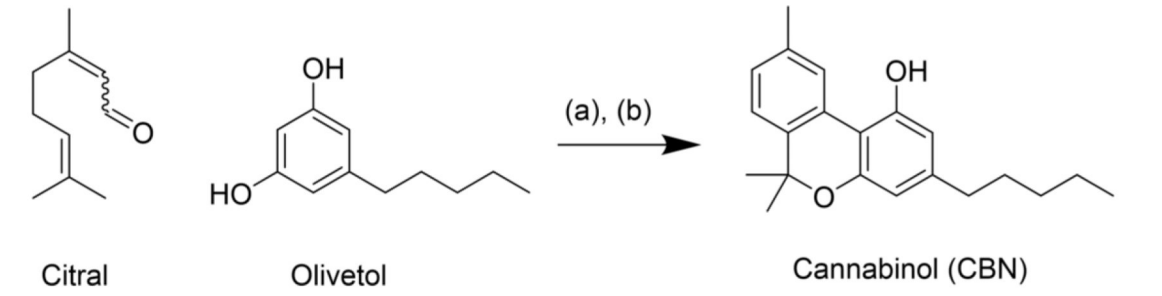

CNS druglikeness for CBN

MW = 310, TPSA = 29, HBD = 1, HBA = 2, cLogD = 6.8, cLogP = 7.4, pKa = 8.2

Figure 1.

Total synthesis of cannabinol (CBN) and its CNS druglike properties. Reagents and conditions: (a) *n*-butylamine, toluene, reflux; (b) iodine, toluene, reflux, 76%. MW, molecular weight; TPSA, topological polar surface area; HBD, hydrogen bond donor; HBA, hydrogen bond acceptor; cLogD, calculated distribution coefficient; cLogP, calculated partition coefficient; pKa, acid dissociation constant.

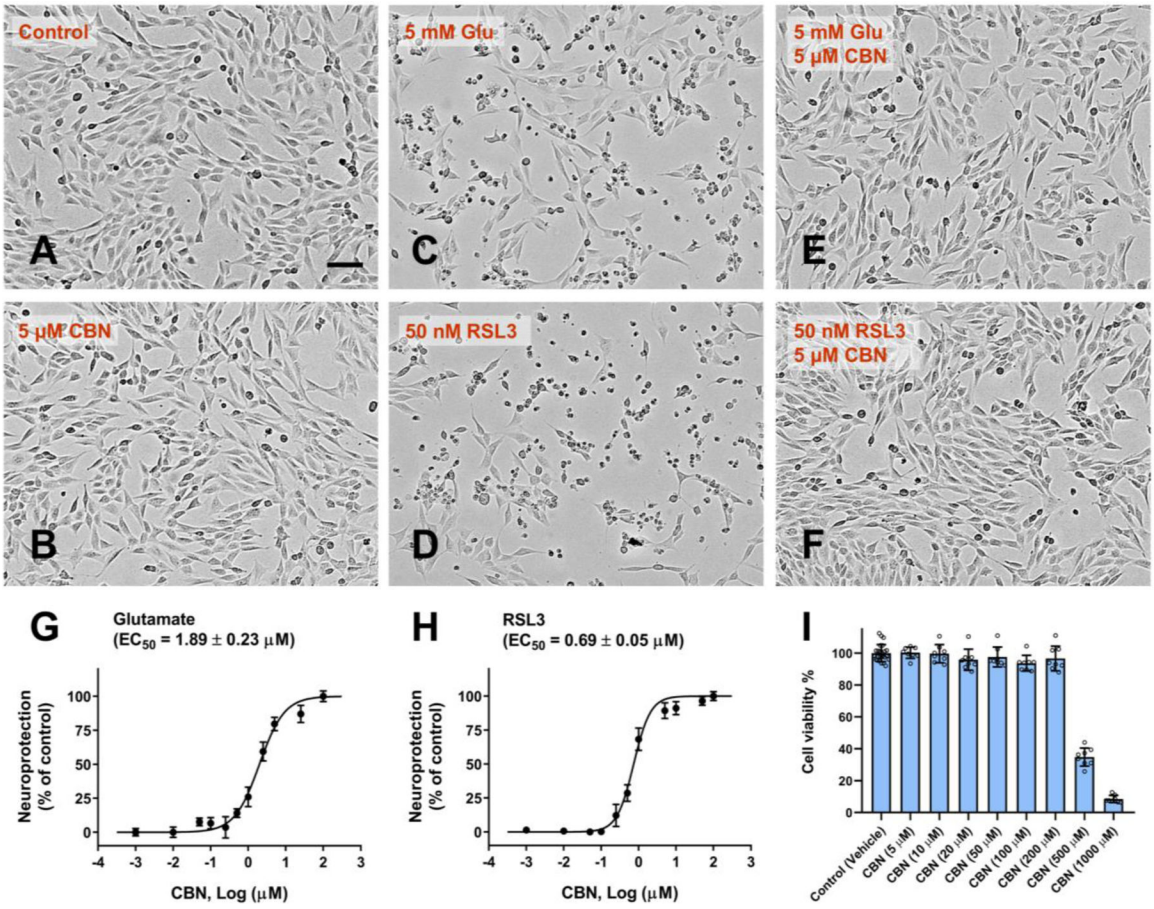

Figure 2.

CBN inhibits oxytosis/ferroptosis in HT22 cells. Representative micrographs of HT22 cells following treatment for 16 hr: (A) 0.2% ethanol treatment as vehicle control, (B) 5 μM CBN treatment, (C) 5 mM glutamate treatment, (D) 50 nM RSL3 treatment, (E) 5 μM CBN pretreatment for 1 h followed by 5 mM glutamate treatment, (F) 5 μM CBN pretreatment for 1 h followed by 50 nM RSL3 treatment. Micrographs show the representative morphological characteristics of the cell cultures under a given condition of 16 experimental replicates. Scale bar = 100 μm. (G) Cells were pretreated with varying concentrations of CBN for 1 hr followed by 5 mM glutamate treatment and incubation for 16 hr. (H) Cells were pretreated with varying concentrations of CBN for 1 hr followed by 50 nM RSL3 treatment and incubation for 16 hr. The results are presented as the percentage of the neuroprotective activity relative to control (100%) and Glu/RSL3 (0%). The neuroprotection curves were analyzed by four-parameter regression. (I) Cytotoxicity assessment of CBN in HT22 cells. Cells were treated with increasing concentrations of CBN or 0.2% ethanol vehicle and incubated for 16 hr. Data are the mean of 8–16 replicates per condition ± SD.

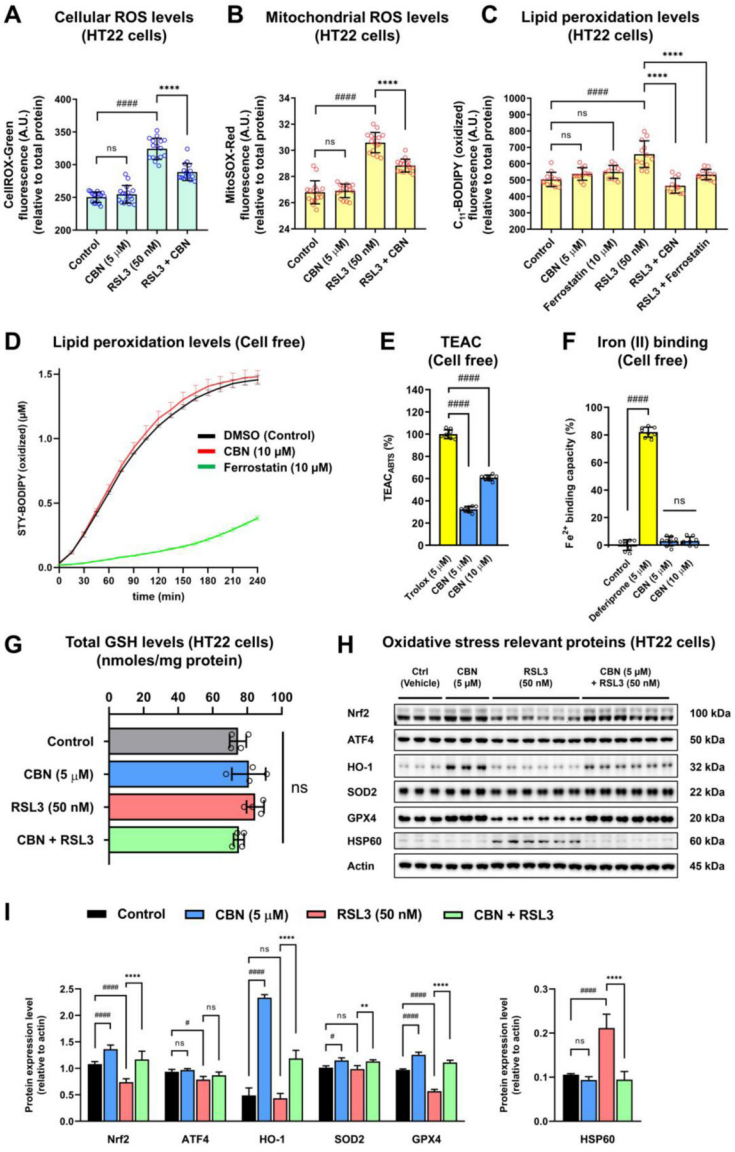

Figure 3.

CBN prevents oxidative stress induced during oxytosis/ferroptosis in HT22 cells. (A) Cellular ROS levels upon different treatment conditions in the cells for 16 hr. Data were normalized to total protein/well and are the mean of 16 replicates per condition ± SD. (B) Mitochondrial ROS levels upon different treatments in the cells for 16 hr. Data were normalized to total protein/well and are the mean of 16 replicates per condition ± SD. (C) Cellular lipid peroxidation levels upon different treatment conditions of the cells for 16 hr. Data were normalized to total protein/well and are the mean of 12 replicates per condition ± SD. (D) Time course of lipid peroxidation levels following different treatment conditions in a cell-free system. Data are the mean of 4 replicates per condition ± SD. (E) Trolox equivalent antioxidant capacities (TEAC) following different treatment conditions in a cell-free system. Data are the mean of 8 replicates per condition ± SD. The results are presented as the percentage of the TEAC relative to Trolox (100%). (F) Iron (II) binding capacities following different treatment conditions in a cell-free system. Data are the mean

of 8 replicates per condition ± SD. The results are presented as the percentage relative to the maximum (vehicle without iron, 100%) and minimum (vehicle with iron only, 0%) Fe^{2+} binding capacity. (G) Total GSH levels upon different treatment conditions of the cells for 16 hr. Data are the mean of 4 replicates per condition ± SD. (H) Western blot data of Nrf2, ATF4, HO-1, SOD2, GPX4, HSP60, and actin (n = 3–6). Protein levels were measured upon different treatment conditions of the cells for 16 hr. (I) Densitometric quantification of the Western blots. Data were normalized to actin and are the mean ± SD. All data were analyzed by one-way ANOVA with Tukey's multiple comparison test. #p < 0.05, ##p < 0.01, ###p < 0.001, ####p < 0.0001 relative to vehicle control; *p < 0.05, **p < 0.01, ***p < 0.001, ****p < 0.0001 relative to the 50 nM RSL3 treatment; ns, not significant.

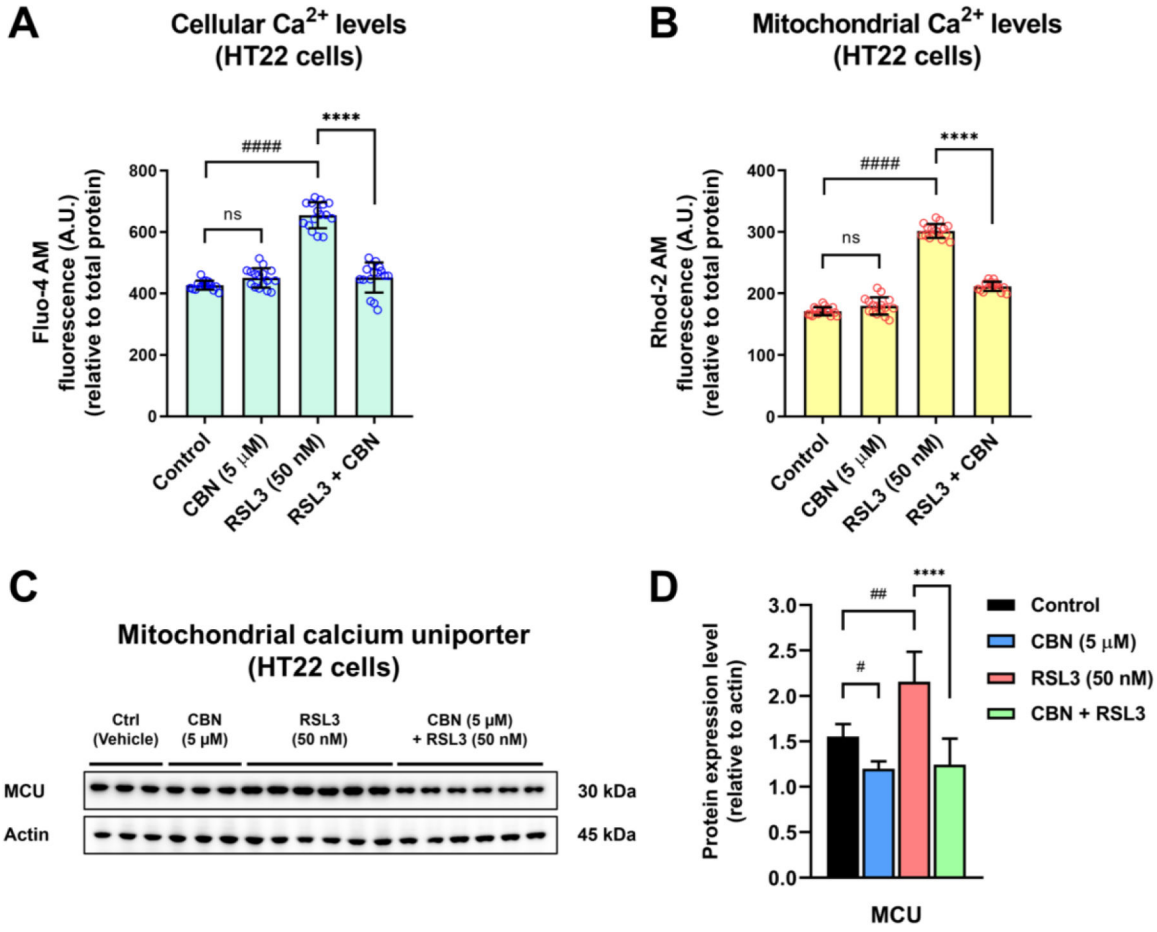

Figure 4.

CBN prevents Ca^{2+} influx induced by oxytosis/ferroptosis in HT22 cells. (A) Cellular Ca^{2+} levels upon different treatment conditions of the cells for 16 hr. Data were normalized to total protein/well and are the mean of 16 replicates per condition ± SD. (B) Mitochondrial Ca^{2+} levels upon different treatment conditions of the cells for 16 hr. Data were normalized to total protein/well and are the mean of 16 replicates per condition ± SD. (C) Western blot data of MCU and actin (n = 3–6). Protein levels were measured following different treatments of the cells for 16 hr. (F) Densitometric quantification of the Western blots. Data were normalized to actin and are the mean ± SD. All data were analyzed by one-way ANOVA with Tukey's multiple comparison test. #p < 0.05, ##p < 0.01, ###p < 0.001, ####p < 0.0001 relative to vehicle control; *p < 0.05, **p < 0.01, ***p < 0.001, ****p < 0.0001 relative to the 50 nM RSL3 treatment.

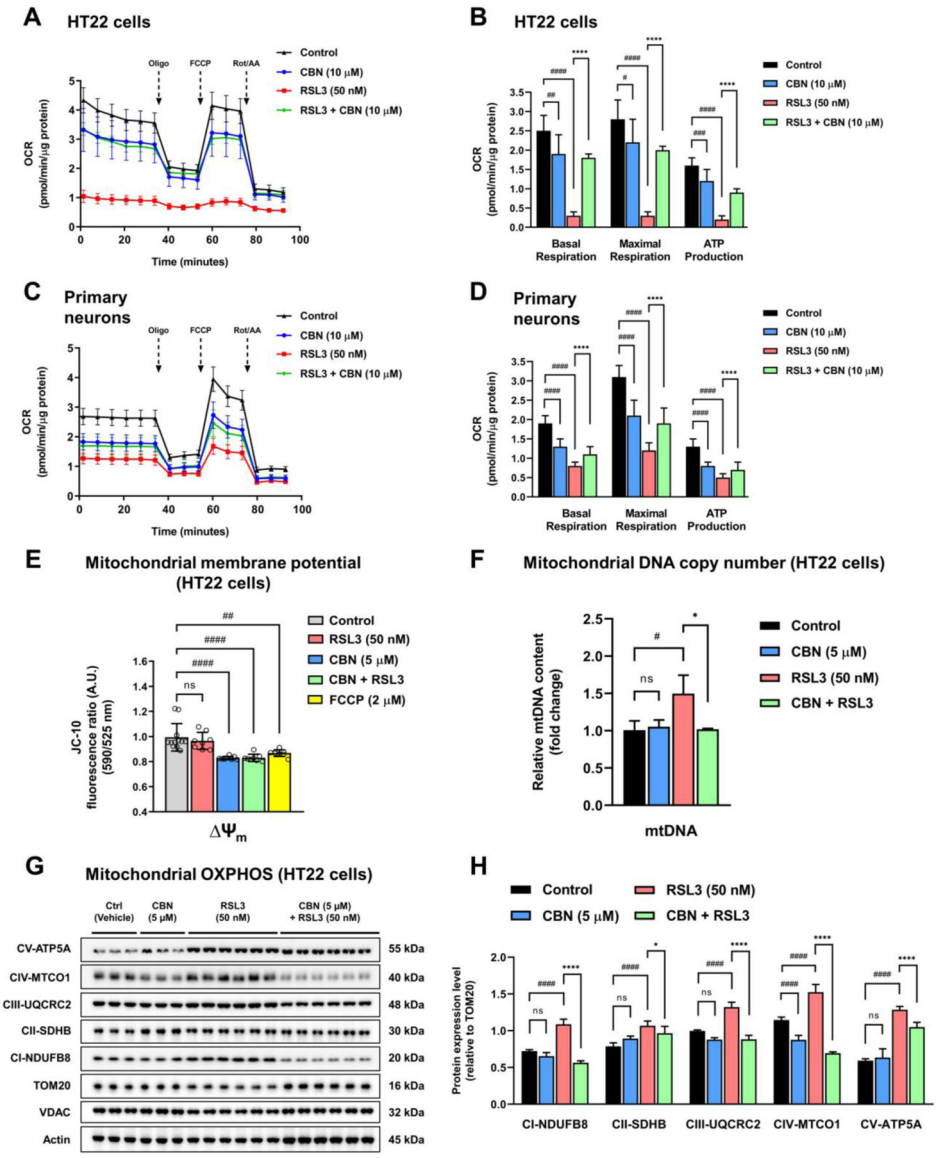

Figure 5.

CBN preserves mitochondrial bioenergetics following induction of oxytosis/ferroptosis. (A) Mitochondrial oxygen consumption rate (OCR) profiles in HT22 cells after different treatments for 16 hr. Data were normalized to total protein/well and are the mean of 20 replicates per condition ± SD. (B) Graphs for basal respiration, maximal respiration, and ATP production in HT22 cells. (C) Mitochondrial oxygen consumption rate (OCR) profiles in primary cortical neurons after different treatments for 16 hr. Data were normalized to total protein/well and are the mean of 20 replicates per condition ± SD. (D) Graphs for basal respiration, maximal respiration, and ATP production in primary cortical neurons. (E) Mitochondrial membrane potential in HT22 cells after different treatments for 4 hr. Data are the mean of 8–12 replicates per condition ± SD. (F) Relative mtDNA copy number in HT22 cells after different treatments for 16 hr. Data are the mean of 3 replicates per condition ± SD. (G) Western blot data of ETC complex proteins (ATP5A, MTCO1, UQCRC2, SDHB,

NDUFB8), TOM20, VDAC, and actin (n = 3–6). Protein levels were measured following different treatments of the cells for 16 hr. (H) Densitometric quantification of the Western blots. Data were normalized to TOM20 and are the mean ± SD. All data were analyzed by one-way ANOVA with Tukey's multiple comparison test. #p < 0.05, ##p < 0.01, ###p < 0.001, ####p < 0.0001 relative to vehicle control; *p < 0.05, **p < 0.01, ***p < 0.001, ****p < 0.0001 relative to the 50 nM RSL3 treatment; ns, not significant.

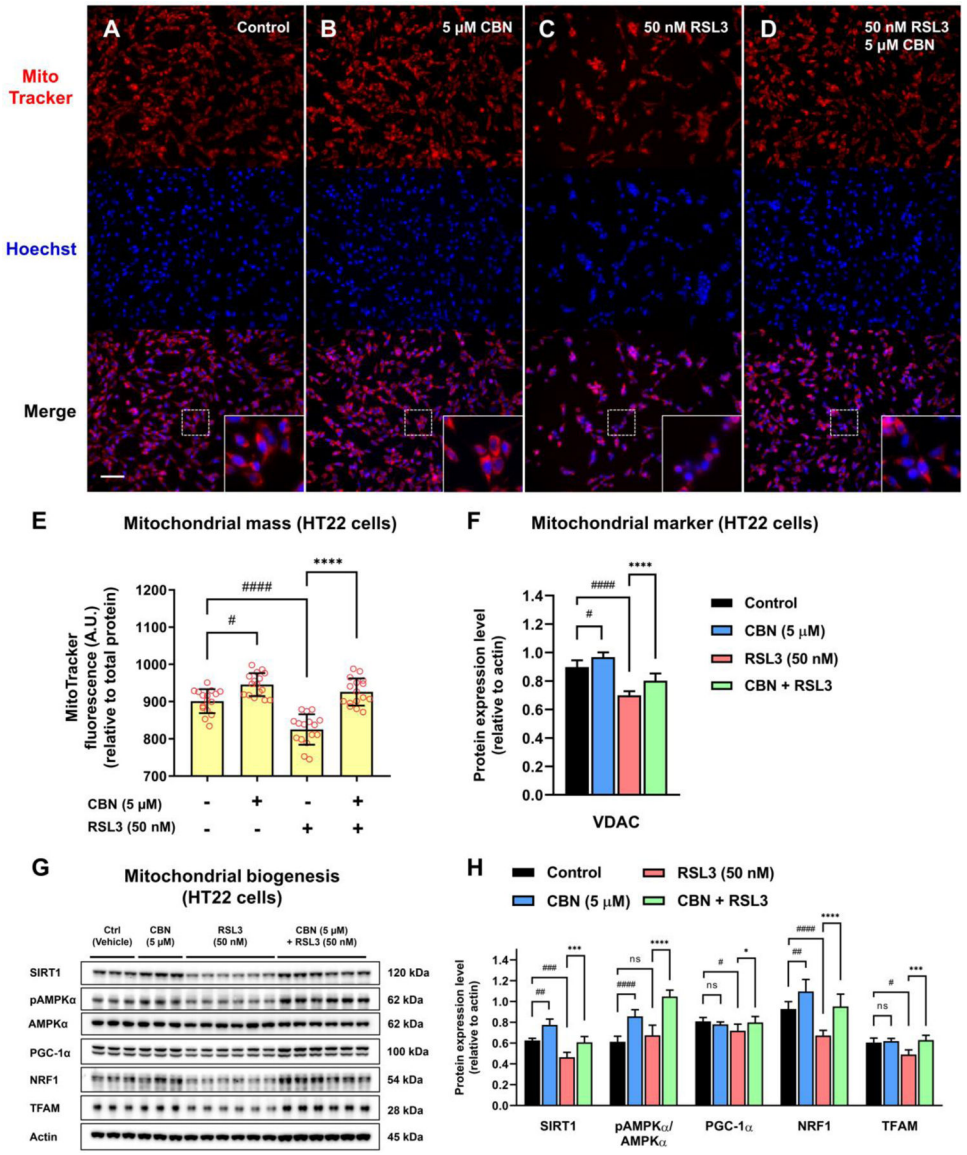

Figure 6.

CBN stimulates mitochondrial biogenesis following induction of oxytosis/ferroptosis in HT22 cells. Representative fluorescent images of HT22 cells following treatment for 16 hr: (A) 0.2% ethanol treatment as vehicle control, (B) 5 μM CBN treatment, (C) 50 nM RSL3 treatment, (D) 5 μM CBN pretreatment for 1 hr followed by 50 nM RSL3 treatment. Mitochondria stained with MitoTracker (red); nuclei stained with Hoechst 33342 (blue). Enlarged images from the boxed areas are indicated. The micrographs show representative morphological characteristics of the cells under the different conditions with 4 experimental replicates per condition. Scale bar = 200 μm. (E) Relative quantification of mitochondrial mass with MitoTracker in HT22 cells following different treatment conditions for 16 hr. Data were normalized to total protein/well and are the means of 16 replicates per condition ± SD. (F) Protein levels of VDAC relative to actin were measured following the different treatments of the HT22 cells for 16 hr using immunoblotting. Data are the means of 3–6

replicates per condition ± SD. (G) Western blot data of SIRT1, pAMPKα (Thr172), total AMPKα, PGC-1α, NRF1, TFAM, and actin (n = 3–6). Protein levels were measured following different treatments of the cells for 16 hr. (H) Densitometric quantification of the Western blots. Data were normalized to actin and are the mean ± SD. All data were analyzed by one-way ANOVA with Tukey's multiple comparison test. #$p < 0.05$, ##$p < 0.01$, ###$p < 0.001$, ####$p < 0.0001$ relative to vehicle control; *$p < 0.05$, **$p < 0.01$, ***$p < 0.001$, ****$p < 0.0001$ relative to the 50 nM RSL3 treatment; ns, not significant.

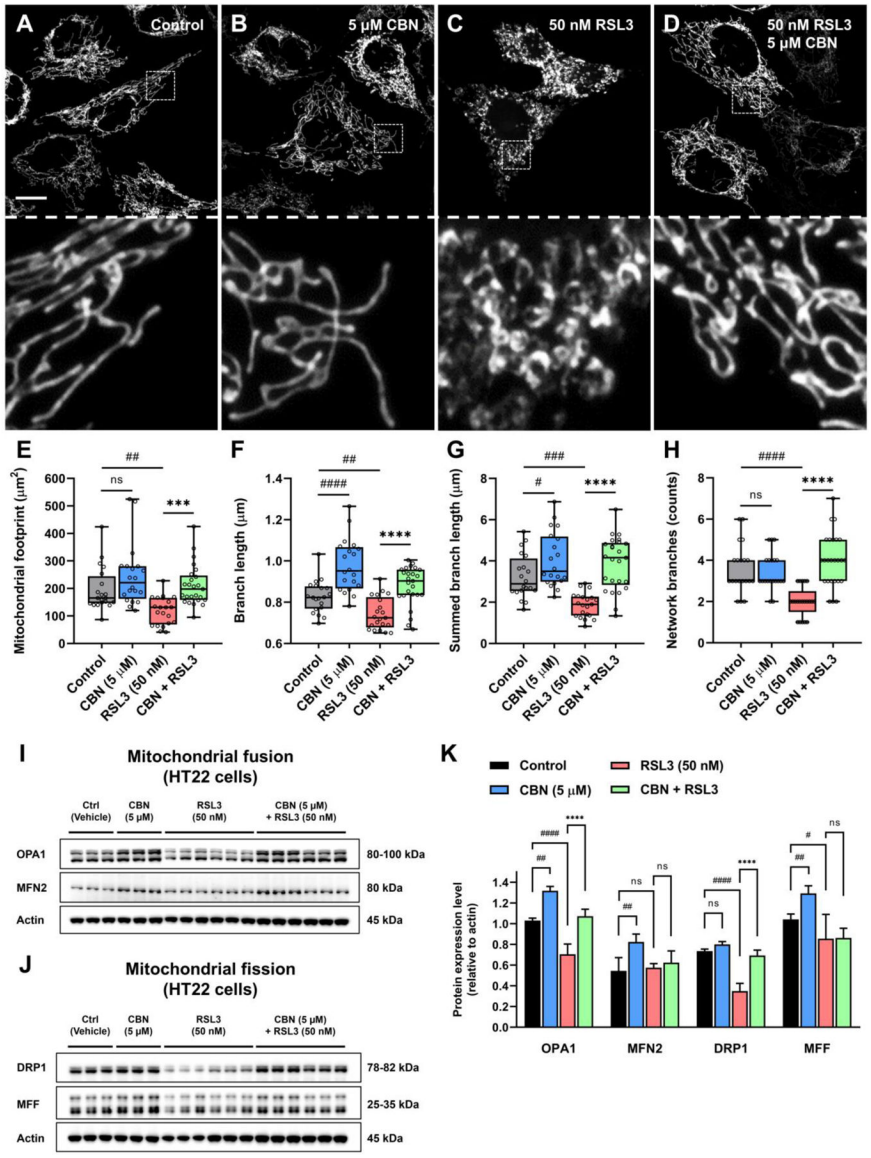

Figure 7.

CBN modulates mitochondrial fusion/fission dynamics following induction of oxytosis/ferroptosis in HT22 cells. Representative fluorescent images of HT22 mt-GFP cells following treatment for 16 hr: (A) 0.2% ethanol treatment as vehicle control, (B) 5 μM CBN treatment, (C) 50 nM RSL3 treatment, (D) 5 μM CBN pretreatment for 1 hr followed by 50 nM RSL3 treatment. Enlarged images from the boxed areas are indicated in the bottom panels. The micrographs show representative images of the morphological characteristics of the cells under the different conditions with 4 experimental replicates per condition. Scale bar = 10 μm. (E) Mitochondrial network morphology analyses on micrographs of HT22 cells after different treatments: (E) mitochondrial footprint, (F) mitochondrial branch length, (G) mitochondrial summed branch lengths, (H) mitochondrial network branches. Data are the mean of 20–25 cells per condition ± SD. (I) & (J) Western blot data of OPA1, MFN2, DRP1, MFF, and actin (n = 36). Protein levels were measured following the different treatments

of the cells for 16 hr. (K) Densitometric quantification of the Western blots. Data were normalized to actin and are the mean ± SD. All data were analyzed by one-way ANOVA with Tukey's multiple comparison test. #p < 0.05, ##p < 0.01, ###p < 0.001, ####p < 0.0001 relative to vehicle control; *p < 0.05, **p < 0.01, ***p < 0.001, ****p < 0.0001 relative to the 50 nM RSL3 treatment; ns, not significant.

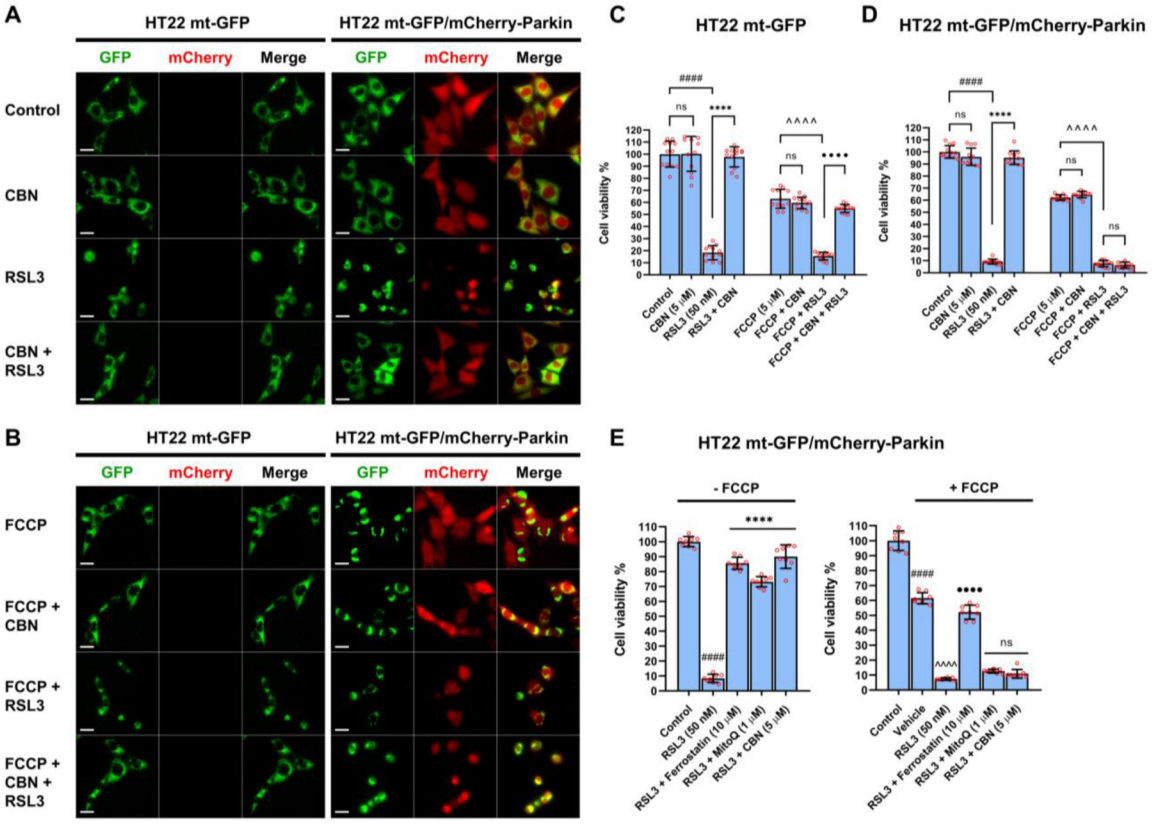

Figure 8.

CBN requires functional mitochondria for protection against oxytosis/ferroptosis in HT22 cells. (A) & (B) Representative fluorescent images of HT22 mt-GFP WT and mt-GFP/mCherry-Parkin cells following the different treatment conditions. GFP-labeled mitochondria (green), mCherry-Parkin (red). FCCP-induced mitophagy in mt-GFP/mCherryParkin cells but not in mt-GFP cells. The micrographs show representative images of the morphological characteristics of the cells under the different conditions with 12 experimental replicates per condition. Scale bar = 50 μm. (C), (D) & (E) DNA-based cell viability analysis of HT22 mt-GFP or mt-GFP/mCherry-Parkin cells following the different treatment conditions. Data are the mean of 8–12 replicates per condition ± SD. All data were analyzed by one-way ANOVA with Tukey's multiple comparison test. ####$p < 0.0001$ relative to vehicle control; ****$p < 0.0001$ relative to the 50 nM RSL3 treatment; ^^^^$p < 0.0001$ relative to the 5 μM FCCP treatment; ●●●●$p < 0.0001$ relative to the FCCP (5 μM) + RSL3 (50 nM) treatment; ns, not significant.

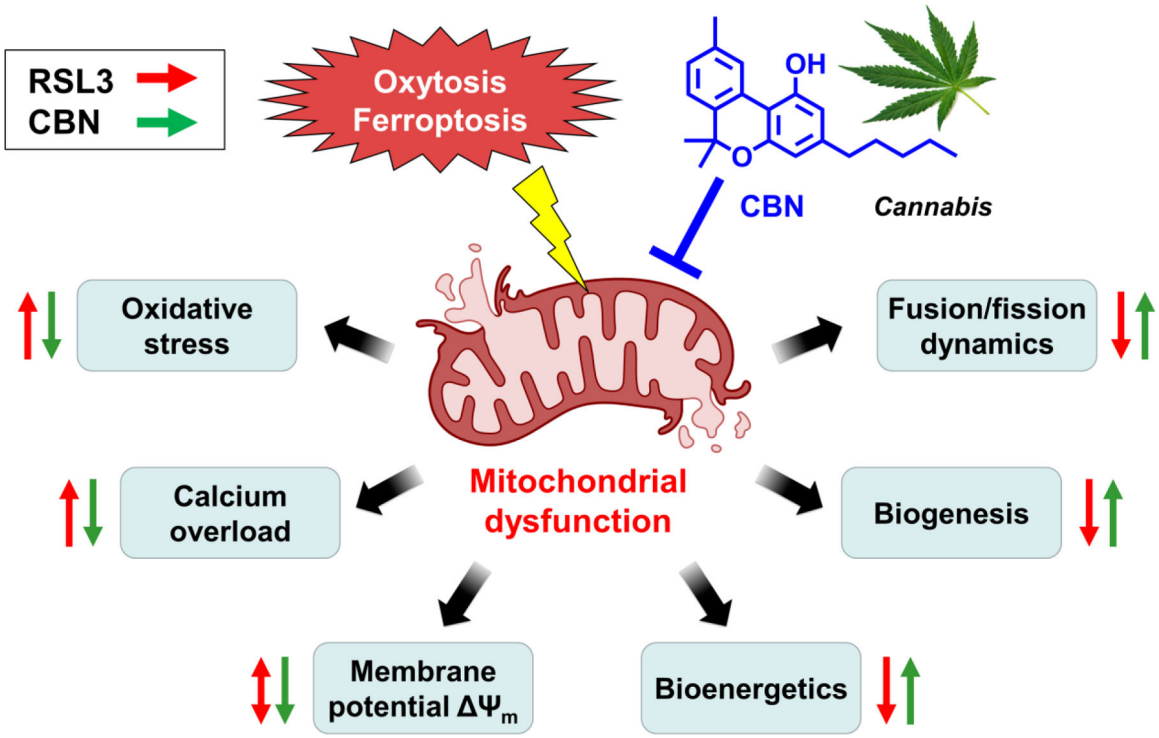

Figure 9.

Proposed neuroprotective mechanisms of CBN against oxytosis/ferroptosis through directly targeting mitochondria to restore multiple key parameters of mitochondrial function. Oxytosis/ferroptosis induced by RSL3 (red arrows) causes an increase in mitochondrial oxidative stress and calcium overload, disturbance of mitochondrial membrane potential, and decrease in mitochondrial bioenergetics, biogenesis, and fusion/fission dynamics. CBN protects neuronal cells through counteracting all these six aspects of mitochondrial dysfunction (green arrows).